Multiscale Fast Fourier Transform homogenization of additively manufactured fiber reinforced composites from component-wise description of morphology[⋆]

Facundo Sosa-Rey[a,*], Clement Vella[a], Alessandra Lingua[a], Juliette Pierre[a], Nicola Piccirelli[b], Daniel Therriault[a] and Martin Lévesque[a,**]

[a] *Laboratory for Multiscale Mechanics, Polytechnique Montréal, Montreal, H3C3A7, Canada*
[b] *Safran Composites, A Technology Platform of Safran Tech, Itteville, 91760, France*

ARTICLE INFO

Keywords:
Multiscale modelling
Short-fiber composites
3-D Printing
X-ray computed tomography
Anisotropy

ABSTRACT

The process-structure-property relation in short-fiber reinforced composites made in Fused Filament Fabrication (FFF) remains inadequately understood, much trial-and-error and extensive testing is required to use these materials for load-bearing applications. As a consequence, the largely empirical design process has hindered the adoption of this technology, notably due to the lack of reliable structural analysis capability. In order to surpass the limitations of mechanical property prediction using simplified artificial microstructures, this work demonstrates the decisive advantage of using geometries obtained directly from imaging of printed specimen instead. The analysis of μCT images is performed via a purpose-built extraction tool called OpenFiberSeg, yielding profound insight into the process-structure relation. The use of real microstructures is shown to considerably improve the mechanical behavior prediction capability via dual-scale FFT-based homogenization, bringing relative error margins below 5%, for full anisotropic description. It also becomes possible to investigate the effect of processing parameters such as nozzle diameter and printing pattern on morphological properties and on mechanical behavior, revealing the magnitude of the spatial variation of local properties. The combination of experimental and simulation enables insight that is not accessible to either alone. Original imaging data and source code are made publicly available.

1. Introduction

Fused filament fabrication (FFF) is an additive manufacturing (AM) method by which complex parts are built layer-by-layer by the deposition of semi-molten polymer filaments through numerical control. As opposed to injection or compression molding, the process requires no molds or tooling, which leads to fewer design restrictions, low cost per unit in small batches, customizability and simplicity of manufacturing [1–4]. By employing short fiber reinforced polymer (SFRPs) filaments made from high-performance polymers such as poly ether-ether-ketone (PEEK) mixed with short carbon fibers (CFs), parts made through FFF exhibit weight-specific properties giving them the potential of replacing metallic components in fields like the aerospace or automotive industries [1, 4, 5]. In addition, by controlling the orientation of reinforcements,

---

[⋆] This research project is funded by the National Science and Engineering Research Council of Canada and Safran Tech.

[*] Corresponding author

[**] Principal corresponding author

✉ `facundo.sosa-rey@polymtl.ca` (Facundo Sosa-Rey); `martin.levesque@polymtl.ca` (Martin Lévesque)
ORCID(s): 0000-0003-1140-0635 (Facundo Sosa-Rey)

the mechanical, thermal and electrical properties of parts can be engineered for specific purposes [1, 3, 6]. However, before FFF parts can be used for load-bearing applications, structural analysis tools must be significantly improved [3, 7, 8]. The lack of understanding of the relation between processing parameters and mechanical properties makes existing tools insufficiently reliable [1, 7, 9], rendering the design process largely empirical [3, 10]. The main problem resides in the fact that morphological characteristics are influenced first by the properties of the base materials and the processing parameters [1, 11–13], which lead to localized gradients in material properties and contribute to suboptimal part consistency [14–17]. Fiber length and orientation distributions, local fiber volume fractions and the formation of porosity are all affected by processing conditions, and exhibit local variation within parts [6, 8, 11, 12, 18, 19]. In addition, parts made by FFF exhibit structural features at several distinct length scales [1, 7], some of which are absent in molded parts [13]. Understanding the link between these microstructural features and the resulting mechanical properties is a crucial, and yet-unsolved, challenge [3, 9, 10, 18, 20, 21].

Generally, three distinct scales are relevant in the context of SFRPs manufactured by FFF. The microscale is where the constituents (matrix, fibers, intra-bead voids) are explicitly considered [7, 11]. Then, the part geometry scale, or macroscale, is always present and is the main focus of mechanical design. Lastly, the FFF process imparts an intermediate, or mesoscale, level of structuring that is determined by the printing infill pattern selected, and the characteristics of the exterior part shell. Even with the simplest of infill patterns, i.e., all passes aligned with each other, and 100% volume occupation, each bead being round at the nozzle tip and forced into a rectangular section leaves voids at the corner of this rectangle, which form a periodic array of neatly aligned cavities throughout the part [1, 21, 22], contributing to part anisotropy [13, 23–25]. All these scales must be encompassed by an attempt to account for the morphology-property relation of AM SFRPs [7].

2. Background

2.1. Morphological characterization: fiber properties

Predicting the mechanical stiffness of SFRPs requires a description of their microstructure, often generated from statistical observations of real materials. Fiber length and orientation distributions are commonly obtained as follows. The elliptical cross-section of individual fibers can be obtained from scanning electron microscopy (SEM) images of polished samples. The orientation of individual fibers in three-dimensional (3D) space are computed by measuring the angle those ellipses make with the printing direction and their ratio of minor to major axis [11, 26, 27]. Fiber lengths can be measured under optical microscopy or SEM after they are separated from the matrix, either though pyrolysis [2, 11] or dissolution [26]. However, those procedures are time-consuming and suffer from repeatability issues [27], and accuracy is reduced for fibers almost perpendicular to the image plane [28]. Further, SEM images are two-dimensional (2D) rather than volumetric, and thus cannot account for property variation at different depths in the material. In addition, the lengths and orientations aren't measured at once on the same fibers, therefore the SEM images method does not produce a full-field description including positions in 3D space, and the correlation between length and orientation is unknown [27]. Some studies have measured this correlation, more so for carbon fibers than for glass fibers because of their higher average aspect ratio [11, 29, 30]. It is possible to obtain data at several depths, by repeatedly polishing the specimen to produce a 3D rendering [27, 31], or use confocal microscopy to image beyond the surface [32].

These statistics can be used directly in analytical modelling [18, 26, 33, 34] or artificial geometries can be tailored to have similar average properties [2, 11, 35–38]. These geometrical descriptions, or representative volume elements (RVEs), are a volume description of a sample of the microstructure which is small enough so modelling is achievable, but rich and complex enough to be representative of the variability of the real morphology (for strict definitions, see [39, 40]). The generation of such RVEs is complex and computationally costly, especially when large fiber aspect ratios and volume filling fractions v_f are required [2, 11, 37, 41]. As a consequence, the v_f considered only rarely reach 25% [38], whereas the v_f in SFRPs are commercially available at 30% and can reach as much as 40% [29, 42]. A commonly used method of microstructure generation is random sequential adsorption (RSA) [14, 38, 43–45], in which inclusions (fibers and/or pores) are seeded into a volume one at a time, checking for interference with existing inclusions, and randomly repositioned in case of interference, until the desired volume fraction is reached. Fiber segments that extend beyond volume boundaries are repeated on opposite faces of the volume, ensuring geometric periodicity [38, 41]. Notably for large aspect ratios, this method has been modified in several ways to enable higher volume fractions [9, 11, 45]. Other methods draw from molecular dynamics modeling, in which fibers have velocities and collide with each other while increasing in volume, until the desired v_f is reached [41, 46, 47]. A few studies attempted generating artificial microstructures with a specific set of orientation and lengths distributions, in addition to infill fractions. Tian et al. proposed a fiber growth method by which they were able to reach 25% of infill [14, 45], but only 19% was achieved with an aspect ratio of 10 [38]. Tang et al. achieved $v_f = 38\%$ at a mean aspect ratio of 15, but only for random orientations [9]. Using a modification of the RSA algorithm, they generated microstructures (including fibers and voids) in which fibers conformed to an orientation tensor obtained from a computed micro-tomography (μCT) scan of a real CF polyamide-12 (PA12) specimen. By generating RVEs with varying characteristics, they demonstrated that fiber alignment has a pronounced effect on tensile properties: an RVE with an average deviation of 18° shows a tensile modulus 2.67 larger than one with random orientation.

Nasirov et al. [2] used artificially generated RVEs with v_f up to 10% with a constant fiber length of 60 μm, with either uniform (random) orientations or aligned with the print direction. This microstructure was homogenized first, then embedded in a mesotructure of unidirectional or 0°-90° printing pattern (each layer has aligned beads, and subsequent layers are perpendicular to each other). For their mesostructure description, the authors considered *ideal* RVEs of beads modelled as rounded rectangles and *actual* RVEs, generated according to mesotructures observed in microscope images of physical specimens. They compared the tensile moduli predicted by simulation to tensile testing measurements performed on carbon fiber reinforced polylactic acid (PLA), and encounter up to 20% error in unidirectional configuration, and up to 40% error for 0°-90°, using actual mesotructure RVEs (error was higher for ideal mesotructures). Another study from the same group considered aligned carbon fibers in polycarbonate (PC), and an ideal mesostructure, and reported 3.5% to 36% error in tensile modulus prediction [22]. These studies suggest the mesoscale porosity has a significant influence on effective properties, notably in making the material anisotropic, even when considering a pure (non-reinforced) isotropic polymer [13]. They also highlight the fact that real microstructures are not perfectly aligned, which has a decisive impact on effective properties. The non-uniform nature of real mesoscale porosity and the probable spatial variation in microscale properties can also cause discrepancies between those models and reality. The correlation between those attributes is also not accounted for. Those factors explain the rather large error encountered when comparing predictions to experimentally measured tensile moduli.

Volumetric characterization based on imaging methods such as μCT has also been reported for SFRPs [8, 19, 27, 29, 48–50]. Obtaining microstructures this way is technically challenging, requiring specialized post-processing that is computationally costly, but the microstructures produced are detailed and high fidelity to physical specimen can be achieved [27, 29, 48]. To the authors' knowledge, however, material data produced in this manner has only rarely [51] been utilized directly for mechanical properties prediction.

2.2. Effect of processing on microstructure

The rheological phenomena by which fiber alignment and lengths are affected by processing has been studied from modelling and expeximental perspectives. Using flow simulations, most studies [33, 52] utilize a so-called weakly coupled approach, in which fluid flow is solved first without considering the presence of fibers. Then, a fiber orientation tensor is inferred from flow profiles via the Advani and Tucker's equations [53].

The weakly coupled assumption is considered valid for $v_f < 10\%$, beyond which fiber-fiber and fiber-matrix interactions induce strong coupling. These models predict a change of fiber alignment at nozzle tip. Lewicki et al. [6] performed flow simulations using discretely modelled fibers and epoxy resin, with a $v_f = 6\%$ and aspect ratio of 50. They found that alignment is promoted during the extrusion phase, most notably close to the walls. Zhang et al. [10] performed a coupled fluids/discrete fiber modelling of extrusion in FFF to study the phenomena of nozzle clogging. They used their modelling and μCT data of CF filled PA6 to propose nozzle geometries and fiber characteristic to prevent nozzle clogging and promote fiber alignment. On the experimental front, Chacón et al. [54] studied the effect of nozzle diameter on the tensile and strength properties of CF reinforced polyamide-6 (CF-PA6) specimens, along with porosity generation and geometric accuracy. They found that mechanical properties increased with a larger nozzle diameter, and that porosity is lowest for large diameter nozzles (measured up to 0.8 mm). However, to the author' knowledge, there hasn't been numerical prediction of mechanical properties taking nozzle diameter as a variable. Extrusion of SFRPs is known to cause fiber breakage, which attenuates their mechanical properties [6, 12, 55]. Limited data exists on this phenomenon, whether experimental [12, 29] or simulated [10], as the computational requirements to model this phenomenon would be prohibitive [3].

2.3. Mechanical property prediction: homogenization

Homogenization is the process of estimating the effective properties of a heterogeneous solid. There are generally two families of methods by which this process is carried out: mean-field and full-field methods. Mean-field, or analytical, methods use statistics about the size and orientation of inclusions along with their material properties to estimate those of the composite solid. Such methods include the Mori-Tanaka [56, 57], the self-consistent scheme [58], Lielen [59] and others, see [36]. These methods all assume ellipsoidal inclusion shapes and uniform spatial distribution of orientations, sizes and local density [60]. Further, the interaction between inclusions is possible only to a limited extent (usually for $v_f < 15\%$) [36, 60]. It has been suggested that these simplifications make mean-field methods unsuitable for modelling complex microstructures such as high-v_f SFRP [38], notably at high property contrasts and aspect ratios [36].

Recent progress in full-field or volumetric approaches have produced more accurate predictions [2, 11, 36, 37, 60], though at a much higher computational cost. In full-field methods, a unit cell representing the microstructure (the RVE) is subjected to external strain, and the local stress response is computed at each point in space by numerical resolution of the constitutive laws. The effective response is obtained by volume averaging of the local responses [18] (see Appendix A for details). The chosen boundary conditions (BCs) directly affect the convergence rate towards true effective properties [40, 45], with periodic BCs converging the fastest [39].

The most well-known of full-field methods is the Finite Element (FE) method, which has had some success in the context of homogenization of SFRPs [11, 14, 38, 45, 51]. However, the FE method requires a suitable mesh representing the microstructure geometry, whose construction becomes increasingly challenging and computationally costly with high v_f [11, 38]. For high fiber content and aspect ratios, the meshing can fail altogether due to numerous contact points between fibers [14, 61]. Mesh-free methods offer a means to circumvent this problem.

One such method was developed by Moulinec and Suquet [62], where the elasticity equation is expressed in a so-called Lippman-Schwinger form, and resolved iteratively with the help of the Fast Fourier Transform operation (FFT) (see Appendix B for details). In the FFT method, the microstructure is described by an orthogonal grid (a 3D array), which means this method has the decisive advantage of being able to use data from 3D-imaging techniques directly [20]. The absence of meshing also lowers the memory requirements, which combined with the computational efficiency of the FFT method, enables the resolution of large and realistic microstuctures [60, 63]. Recent developments have extended the original Moulinec and Suquet method to allow convergence in presence of infinite phase contrast (as for porous materials), which was a limitation of the original formulation [64]. The AMITEX software implements the FFT method with these improvements, along with distributed computing techniques that allow performance gains on multi-CPU architectures [65, 66].

When a material exhibits structuring phenomena at dissimilar length scales, such as in SFRPs made by FFF, attempting to consider the smallest features at the largest scale is often unfeasible [20, 67]. Sommireddy et al.[51] attempted it for predicting tensile properties, using a single RVE with a simplified description of both micro and mesostructure, with error margins of 16 to 26%, depending on load direction. Multiscale techniques are used instead, where the constitutive equations at the macroscale are substituted by the output of the boundary value problem computed at the microscale. Doing so allows the combination of different methods for each scale, drawing on the strengths of each. For instance, the efficiency of FFT method applied to the microscale can be combined by the ability of FE at the macroscale to account for arbitrary part geometry and BCs [60, 63]. For the multiscale method to be valid, however, a sufficient scale separation must exist between the each scale: the typical length at which the smallest features vary, or l_n, must be small when compared to the RVE size used to homogenize those features, or L_n. That RVE size must also be small when compared to the features at the scale above it, or l_{n+1}, and the RVE size used to model those, or L_{n+1} [68]. This can be expressed as $l_n << L_n << l_{n+1} << L_{n+1}$.

3. Methods and materials

We investigated the process-structure-property relation of SFRPs made by FFF. As shown in Figure 1, specimens of CF reinforced PEEK were manufactured using unidirectional (0°-0°), 0°-90° and 90°-90° patterns and an intermediate nozzle diameter. Unidirectional specimens were also fabricated for 2 additional nozzle diameters, one smaller and one larger. As shown in Figure 2, for each scenario, both the microscale and mesoscale morphologies were characterized through μCT imaging. Component extraction was then performed using OpenFiberSeg, a special-purpose tool developed by the authors [29]. This tool enables the identification of individual fibers, as well as the intra-bead (microscale) and inter-layer (mesoscale) porosity. Sub-volumes where no mesoscale features are present are located, which serve as representation of the intra-bead microstructure itself. This microscale description $\mathbf{C}(\mathbf{x})$ (stiffness as a function of position in space) was then processed with the AMITEX software to obtain an homogenized effective stiffness at the microscale, $\tilde{\mathbf{C}}_{\text{micro}}$, which was used in turn to obtain the homogenized stiffness at the mesoscale, or $\tilde{\mathbf{C}}_{\text{meso}}$. The stiffness predicted by dual-scale homogenization was then validated by comparing with experimental data and contrasted with predictions made with simplified artificial microstructures.

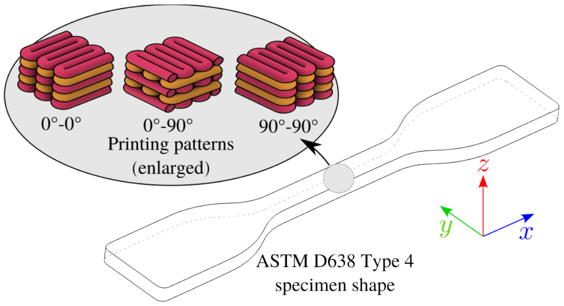

Figure 1: Schematic representation of the printing patterns used to produce the test specimens. For all nozzle diameters, the 0°-0° or unidirectional along the longitudinal axis was studied. For the 0.4 mm nozzle, additional specimens using the 0°-90° and 90°-90° pattern were also considered.

3.1. ASTM D638 Type 4 specimen preparation

Commercial filament Tecafil™ PEEK VX 30CF from Ensinger was placed in a vaccum oven for 24 h at 60°C and 17 kPa. Figure 1 shows an ASTM D638 Type 4 dogbone specimen that was printed in an AON3D™ Mark 2 industrial 3D printer using 3 different nozzle diameters (Volcano model from E3D, diameters $D = 0.25$, 0.4 and 0.8 mm). The slicing parameters utilized in the Simplify3D™ slicer are shown in Table 1. The layer height and extrusion multiplier were set empirically by attempting to minimize inter-layer porosity, with a printing speed of 30 mm/s. In addition, the following temperature settings were common to all specimens: nozzle temperature: 410°C, bed temperature: 180°C, and chamber temperature: 120°C (maximum allowable in AON Mark 2). A total of 6 specimens were produced for each nozzle diameter,

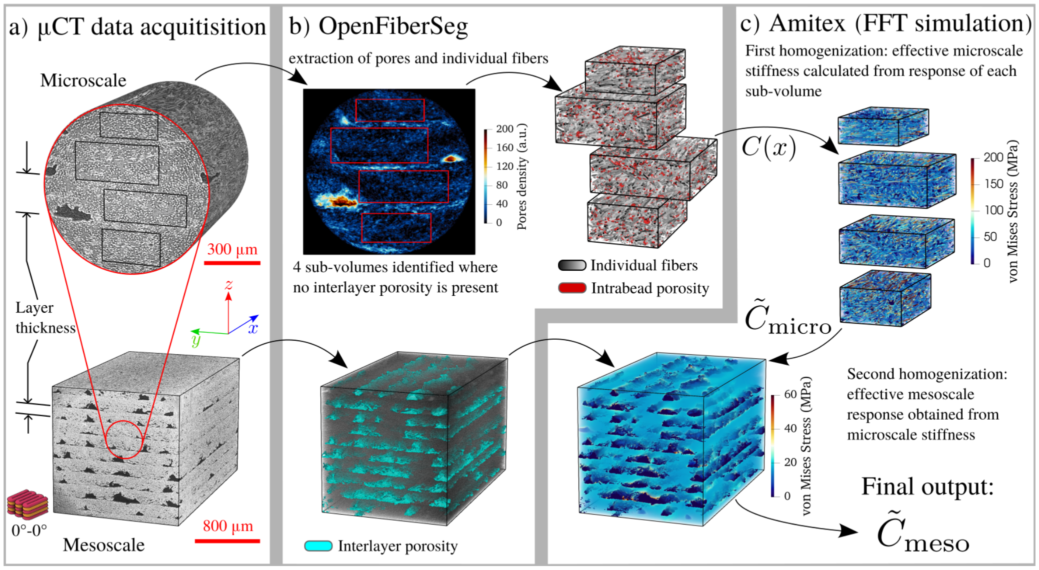

Figure 2: Schematic flowchart of the dual-scale FFT-homogenization. a) μCT imaging data of physical specimen, performed with large field of view for the mesoscale, and at high resolution for the microscale. b) Constituent extraction using specialized software OpenFiberSeg. c) The result of FFT-homogenization at the microscale serves as input for the mesoscale homogenization.

Table 1
Printing parameters used for each specimen type

D, nozzle diameter (mm)	Layer height (mm)	Extrusion width (mm)	Extrusion multiplier	Printing pattern
0.25	0.10	0.22	0.95	$0° - 0°$
0.40	0.20	0.42	1.10	$0° - 0°, 0° - 90°, 90° - 90°$
0.80	0.25	0.80	1.01	$0° - 0°$

using longitudinal or 0°-0° (all passes are along the longitudinal axis of the specimen, i.e., the 0° direction). Using the 0.4 mm nozzle, 6 additional dogbones were made using a 0°-90° pattern (layers alternate printing passes along the long and short axis) and a 90°-90° pattern (all passes perpendicular to the dogbone axis). Filaments spools were kept in the heated chamber for the duration of printing.

Additionally, for each of the nozzle diameters considered, 3 specimens were made by extrusion in free-space, meaning the printhead is not pressed against the table. These specimens enable the characterization of the microstructure at the bead scale, excluding all phenomena related to the deposition onto a part.

3.2. Tensile testing

The specimens were loaded at a rate of 5 mm/min using a MTS Insight Material Testing system and a MTS uniaxial extensometer model 634_25F-25. For each loading sequence, the strain was obtained directly from the calibrated extensometer readings, and the stress was computed by dividing the loading force by the specimen cross-section area (measured from the average of 4 caliper measurements along the narrow section of the dogbone). The linearly elastic range for each specimen was identified in the following manner.

A first-degree polynomial was fitted by the least-square method to the entire stress-strain data. The fit was then performed iteratively, each time removing the point at the highest stress from the data, until the relative error between the fitted line and the experimental curve reached 1%. This segment of the data was considered within the linear regime, and the tensile modulus for each specimen is the slope of the fitted line.

3.3. Volumetric characterization

3.3.1. Tomographic data acquisition

Using a specimen of roughly the same physical dimensions as the scanning field of view (FoV) minimizes the noise contributed by material outside the FoV and helps achieve the highest quality imaging data. To ensure that individual fibers are differentiated and tracked, at least 10 pixels [8, 29] for the typical fiber diameter of $7 - 10$ μm are required for carbon fibers, which leads to a pixel size of $0.7 - 1.0$ μm. The Zeiss XRadia™ 520 micro-tomographic scanner has a cylindrical FoV with a diameter and height of ~ 1000 pixels, which at that pixel size allows for a diameter and height of $0.7 - 1.0$ mm of physical specimen volume. In each specimen, a roughly cylindrical section of diameter $1 - 1.5$ mm was manually carved from the narrow part of the dogbones and mounted on the specimen holder. The following scanning parameters were used: source power: 7 W, source voltage 80 kV, distance from source to specimen: 9.1 mm, distance from detector to specimen: 23.0 mm, optical magnification: 10×, exposition time: 1.25 s, number of projections: 3200, and no filter (i.e., using air attenuation). This configuration yields a pixel size of 0.764 μm, and a total scan time of 2 h 20 m per specimen. Two separate FoVs were chosen inside each specimen to account for local variations in properties. In total, 4 FoVs were scanned at high resolution for each printing configuration: 2 FoV per specimen and 2 specimens per configuration. The free-space specimens, along with a section of feedstock 1.75 mm filament, were also scanned in this manner.

Except when using the nozzle with $D = 0.25$ mm, the grid-like printing pattern is larger than the diameter of the high resolution scans. To enable the analysis of those mesoscale features, rectangular sections measuring ~ 4 mm on one side were also produced and scanned at a larger FoV (meaning at a lower resolution). Here, the scan resolution was reduced considerably since we are mainly interested in the larger mesoscale porosity, not the small intra-bead pores, nor the fibers. The parameters used are the same as above, except for: distance from source to specimen: 21.1 mm, distance from detector to specimen: 9.0 mm, optical magnification 4×, exposition time: 0.4 s, number of projections: 1600. This yielded a pixel size of 4.69 μm and a total scan time of 40 min. One such FoV was produced for each nozzle diameter and print configuration. As the specimen preparation for μCT scanning is destructive (a small section is carved from the dogbones) all imaging was performed after tensile testing.

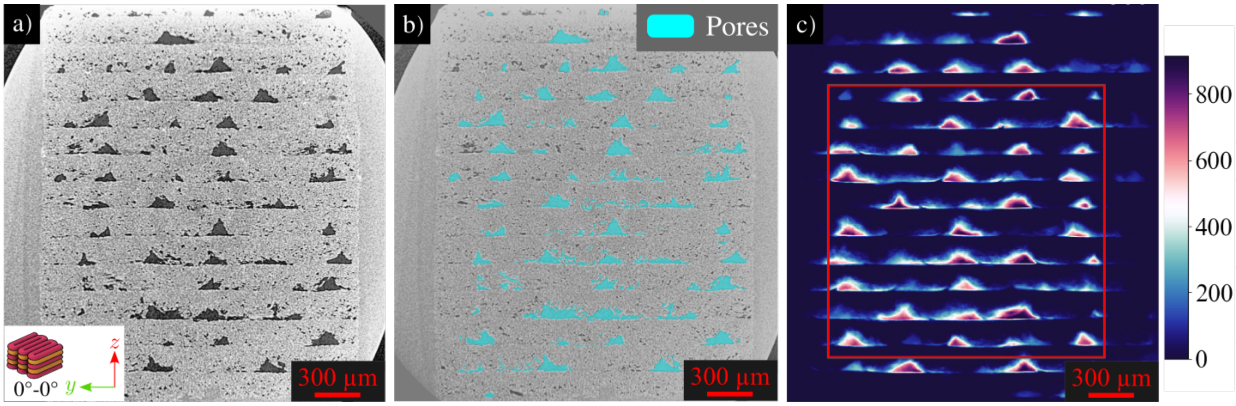

Figure 3: Segmentation of mesoscale porosity and definition of subvolume for homogenization. a) Slice of tomographic data showing a rectangular specimen printed according to the 0°-0° pattern and a 0.4 mm nozzle. Horizontal printing layers are visible, leaving mesoscale porosity in dark. b) The inter-layer porosity identified by OpenFiberSeg is highlighted in light blue. c) Cumulative sum of all porosity voxels in the out-of-plane direction. The grid-like arrangement of printing passes is revealed in sharp contrast. The red rectangle is the chosen subvolume for homogenization.

3.3.2. Component extraction (OpenFiberSeg)

The tomographic scans were processed with the help of OpenFiberSeg, an open-source software built for the purpose of identifying the constituents in the volume (matrix, pores and individual fibers). With this software, the user first manually labels a small patch of data to identify the constituents. This labelling is then fed to a machine learning algorithm to identify the remaining pixels in the entire dataset. On a slice-by-slice basis, the pixels containing fibers are automatically grouped into connected regions, and the centroids of those regions are tracked across 3D space to form neatly aligned chains, which are used to infer the presence of individual fibers. Thanks to this extraction, it is possible to build a voxel-based (regularly-spaced volume elements) representation of the microstructure for a specific specimen. Porosity is labelled using classical image processing methods such as the Canny edge detection algorithm. As can be seen in Figure 3 a), at this length scale, the large pores belonging to the mesostructure and the smaller intra-bead pores can be discriminated according to their size. Each pore size is estimated by the number of connected pixels it contains, then a size threshold ($\sim 1\%$ of total FoV volume) was chosen such that only mesoscale porosity is kept. Examination of Figure 3 b), in which the pores above the threshold are in shown in light blue serves to ascertain that all the mesoscale porosity has been labelled.

3.3.3. Subvolume definition, micro and mesoscale

For the purpose of homogenization, one or more rectangular subvolumes inside the cylindrical FoV need to be identified. These combined subvolumes form the RVE for a particular printing configuration. The FoV must be cropped for several reasons. First, the rectangular subvolume must lie entirely within the material. Then, for the case of mesoscale homogenization, the subvolume dimensions should respect the periodic structure formed by the evenly spaced printing layers and extrusion beads, since only a handful of periods is included. Lastly, for the purpose of dual-scale homogenization, the microscale structure containing fibers/matrix/intra-bead pores must be isolated from the mesoscale pores, to not skew the results by including those twice.

The shape and size of porosity made by the priting pattern is irregular and the grid-like pattern is not readily visible on a single slice. To reveal this pattern more clearly and to identify suitable subvolumes within a FoV, the following method was used. Across the entire volume, the pixels containing pores were assigned the value 1, and all other pixels the value 0. Then, we took the cumulative sum of all 2D slices in the volume along a reference direction (for instance, the out-of-plane direction in the Figure 3 b), creating a 2D map with high values where the mesoscale porosity in concentrated, and low values otherwise, as shown in Figure 3 c). Here, the mesoscale porosity is revealed unambiguously for the entire volume. A subvolume that is inscribed in the natural periodicity of the mesostructure is thus identified: the red rectangle in Figure 3 c) encompasses an integer number of layers (starts and ends at mid-layer in the vertical direction) and of passes (starts and ends at bead centers).

The same projection procedure was repeated for the case of microstructure homogenization, on the high-resolution imaging data, as shown in Figure 4 for the nozzle with $D = 0.4$ mm and a specimen made with a 0°-0° pattern. In Figure 4 a), the input imaging data is shown, with the corresponding material labelling in Figure 4 b). In Figure 4 c), the subvolumes identified are the largest possible such that they contain only microscale porosity.

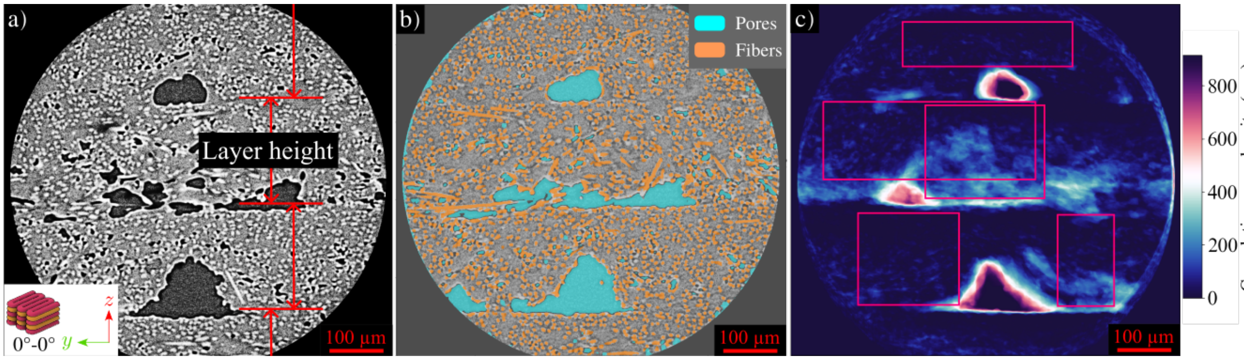

Figure 4: Segmentation of fibers and microscale porosity and definition of subvolumes for homogenization. a) Slice of tomographic data of a specimen printed according to the 0°-0° pattern with a 0.4 mm nozzle, showing horizontal printing layers. b) Fibers and porosity found by OpenFiberSeg highlighted in orange and light blue, respectively. c) Cumulative sum of porosity voxels in the out-of-plane direction. The location of mesostructure porosity across the volume is made obvious, relatively to the single-slice rendering in b). The red rectangles are chosen for homogenization, selected to the maximum size while avoiding mesoscale porosity.

Table 2
Material properties for base constituents, see [69, 71, 72].

Polymer	E (GPa)	ν	**Carbon fibers**	E_l (GPa)	E_t (GPa)	ν_l	ν_t	G_l (GPa)
Victrex 450G PEEK	4.0	0.3855	Toray T300	230	13.4	0.256	0.3	27.3

3.4. Dual-scale homogenization

Under the condition of scale separation, the microscale morphology (including fibers, matrix, and the small, inter-layer porosity) can be homogenized by itself if the scale at which this homogenization occurs (a single pass) is large when compared to the dimension of constituent phase change (the size of fibers and pores). Using many subvolumes across several different scans enables the estimates given by homogenization to be representative of the variability in the real material.

The AMITEX software accepts as inputs a volumetric description containing a number of different materials, which can be the organized in zones, for instance for fibers or grains with different orientations. For the problem at hand, the isotropic matrix is described by tensile modulus E and Poisson's ratio ν. If the axis of the transverse isotropy is $\vec{e}_1$, and the transverse plane is $\vec{e}_2 \times \vec{e}_3$, the fibers are described by longitudinal (along $\vec{e}_1$) and transverse (along $\vec{e}_2$ or $\vec{e}_3$) moduli E_l and E_t, respectively, Poisson's ratios between axes ($\vec{e}_1$,$\vec{e}_2$) and ($\vec{e}_2$,$\vec{e}_3$), i.e. ν_l and ν_t respectively, and the shear modulus between axes ($\vec{e}_1$,$\vec{e}_2$), i.e. G_l. The matrix properties were obtained from manufacturer datasheets on Victrex 450G PEEK [69]. The precise carbon fiber type is not disclosed, but the most likely candidate are the so-called standard modulus fibers, of which Toray T300 carbon is the most common and cost-effective [70]. The material properties for T300 fibers are taken from [71, 72]. Property values are given in Table 2.

Whereas all matrix and porosity voxels can share the same default zone (they are isotropic), the different fiber orientations are represented using zone descriptors at each voxel, which include a rotated reference frame onto which the stiffness tensor is projected. The implementation of the AMITEX software has the number of zones limited to $2^{15} = 32768$. For large subvolumes containing more fibers than this limit, the orientation angles ϕ and θ (spherical coordinates) are rounded to the nearest integer, and fibers with common angle pairs are grouped under the same zone identifier, with negligible effect on homogenization output (this was tested on subvolumes below the fiber count limit, for which it is possible to not round the angle values).

The homogenized stiffness tensor for an equivalent solid is obtained by subsequently applying the uniaxial strains in the 3 references directions, and the 3 pure shear strains to a given microstructure. For each load case, the volume-averaged stress response of the entire solid yields one column vector in the homogenized stiffness tensor for this material (see Appendix A for more details). For each printing configuration, each subvolume is processed through AMITEX in this manner, and the stiffness tensors for each realization were averaged. This averaged tensor represents the composite made of matrix-fiber-microscale pores, which is then used in mesoscale homogenization, where the RVE contains this composite and the grid-like porosity pattern due to the printing procedure. For the 0°-90° printing pattern, the microscale was homogenized separately for beads containing only 0° or 90° subvolumes, and the two resulting $\tilde{\mathbf{C}}_{\mathrm{micro}}$ were averaged together to represent the 0°-90° pattern. Only then was inserted into the mesostructure RVE. The output of this last stage is the effective stiffness for each printing configuration.

The specimen made with the $D = 0.25$ mm nozzle has a printing pattern with layer height × extrusion width of 0.1 mm×0.2 mm. As such, a single high-resolution scan volume of $\varnothing\approx0.75$ mm contains several printing passes, so in this case only single-scale homogenization is required.

3.5. Alternative approach: artificial microstructures

The approach based on high-resolution tomographic imaging is restrictive in many respects. It requires access to expensive equipment and technical expertise, and extensive post-processing of the imaging data. To benchmark the quality of our modelling approach against those found in the literature [2, 22], and quantify its added value, the following approach is also presented. Producing an artificial geometry with the full orientation and lengths distribution of real materials, at high v_f is technically challenging, and beyond the scope of this work. Much like the approach used in [2, 22], a simplified set of artificial geometries can be used instead. Based on the work of Ghossein et al. [41], microstructures can be created using an algorithm based on molecular dynamics modelling, in which ellipsoidal fibers are generated at a fixed aspect ratio (AR), with near-ideal alignment (some fibers rotate during the generation process due to collisions), up to a desired v_f. Spherical pores, occupying a specified volume fraction $v_p =$ are also produced. To determine which AR is representative of a real physical specimen, the following method was used. In Figure 5 a), the distribution of lenghts and deviation angles θ as seen in real physical specimens is shown. Longer fibers contribute more to the effective stiffness than shorter fibers, therefore simply using the mean length as seen in a real specimen will not capture the outsized effect of longer fibers. An estimation of the effect of AR on effective properties was gained by performing Mori-Tanaka simulations on aligned microstructures, for AR ranging from 1 to 100.

In Figure 5 b), the relative effect (or weight) of a fiber's AR is shown: by keeping v_f constant, the tensile modulus predicted by the Mori-Tanaka model is normalized by the modulus for $AR = 1$. The value obtained is an indication of the effect each AR has on the effective moduli: an AR=10 was a weight of 3, meaning it has 3× the effect on effective stiffness than a fiber of AR=1. Using these weights, a weighted mean can be computed, which accounts for the larger effect of longer fibers. For instance, instead of one fiber with AR=1

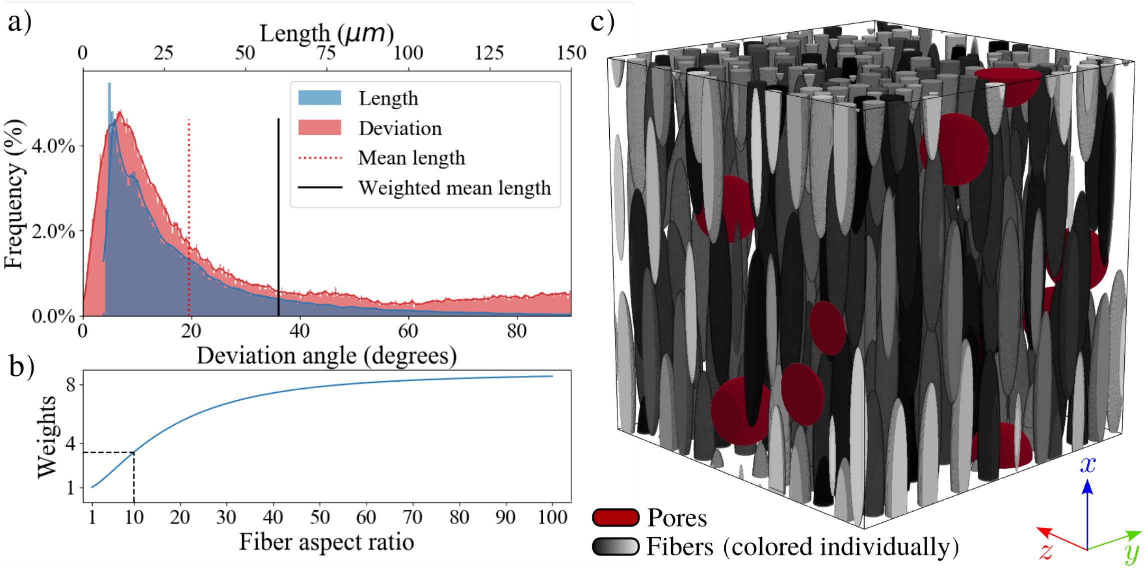

Figure 5: Generation of representative simplified artificial microstructure. In a) the fiber lengths and deviations in all physical specimen is shown. In b) the Mori-Tanaka model is used to give a weight to each fiber according to its aspect ratio, and its relative impact on effective tensile properties. c) Example of a microstructure, with constant aspect ratio $AR = 8$, corresponding to the weighted mean in b), and near-ideal alignment. This RVE was used to compare against the prediction accuracy of the homogenization procedure using imaging data. Fibers occupy $v_f = 23.1\%$, and pores occupy $v_p = 2\%$, which is consistent with real material microstructures.

and one with AR=10 giving a mean AR of 5.5, we consider the fiber with AR=10 to be duplicated 3 times, according to its weight, therefore the weighted mean becomes $(10*3+1)/4 = 7.8$. Therefore, a Mori-Tanaka estimate using two fibers with AR=1,10 is equivalent to one with a single fiber of AR=7.8, keeping total v_f constant. The weighted mean procedure is done on the distribution of ARs in a real specimen, duplicating each fiber by the integer amount of its weight. The weighted and unweighted mean obtained are presented in Figure 5 a), with values of 32 μm ($AR = 4.2$) and 60 μm ($AR = 8.0$), respectively.

The latter value of AR is used to generate artificial microstructures, along with $v_f = 23.8\%$ and $v_p = 2\%$, and a deviation value $\theta \approx 0°$. As these microstructures are costly to generate for large fiber counts, 20 subvolumes with 300 fibers and 8 pores were used instead. An example of such a microstructure is presented in figure 5 c), with fibers identified in different shades of grey, and pores shown in red. Keeping the same dual-scale FFT-homogenization approach, these artificial geometries are used as a stand-in for the microscale description from real materials. The averaged output of this homogenization ($\tilde{\mathbf{C}}_{\text{micro}}$) was then inserted into the same mesoscale RVE obtained from μCT imaging of each specimen type, to evaluate the relevance of using high-resolution imaging and individual fiber tracking. The alternate approach uses only the low-resolution μCT images for the mesoscale, and the much simpler labelling of mesoscale porosity, along with idealized microstructure description.

Table 3
Measured averaged modulus for each specimen type, with 95% confidence intervals

D, nozzle diameter (mm)	Printing pattern	Averaged modulus (GPa)
0.25	$0° - 0°$	19.4 ± 1.0
0.40	$0° - 0°$	16.4 ± 0.7
0.80	$0° - 0°$	18.5 ± 1.0
0.40	$0° - 90°$	9.7 ± 0.6
0.40	$90° - 90°$	3.2 ± 0.3

4. Results and discussion

4.1. Tensile testing results

Figure 6 contains the stress-strain curves as measured during tensile testing, as well as the line segments that represent the estimated linear domain for each test. In general, considerable variability is observed between specimens of the same printing configuration.

The averaged modulus for each specimen category is presented in Table 3. Among the specimen made with the 0°-0° print pattern, those made with the $D = 0.4$ mm nozzle have a stiffness 14% lower than the average of specimens made with the $D = 0.25$ and 0.8 mm nozzles. The specimens made with the 90°-90° pattern have the lowest tensile modulus, since the fibers are mainly oriented in the direction perpendicular to the testing direction, and the specimens at 0°-90° exhibit an intermediate modulus.

4.2. Effect of nozzle diameter

The probability density functions (PDF) of fiber lengths and deviation angles from the extracted fiber properties pertaining to the free-space extrudates and the segment of 1.75 mm filament feedstock are shown in Figure 7. In Figure 7 a) the extent of fiber breakage is revealed: for all 3 nozzles, the proportion of fibers shorter than 20 μm increased by nearly a third, when compared to that of the 1.75 mm filament, with

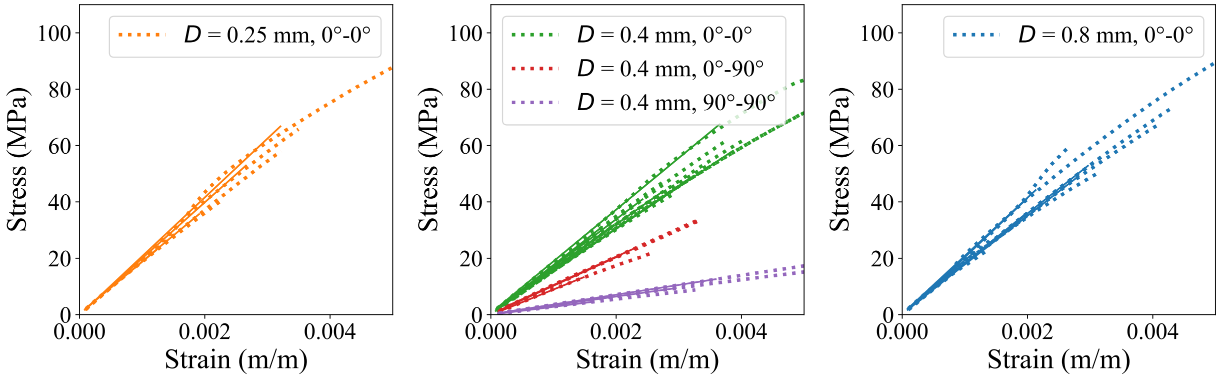

Figure 6: Stress-strain curves for each specimen, for all 5 printing configurations. Solid lines segments represent the estimation of the linear elastic domain for each curve, from which the tensile modulus is calculated.

no large distinction between nozzle diameters. In Figure 7 b), the effect of extrusion on fiber alignment is appreciated, as measured by the peak locations (θ_{max}) on each curves and the measure of full width at half maximum (FWHM). Although the position of peaks is nearly unchanged, there is more dispersion surrounding the peak in all extruded specimens. Though these variations are small, their magnitude had not been measured before. Having these distributions along with the corresponding 3D renderings of the fibers as they present in each bead could be valuable for future rheology modelling efforts of the extrusion of SFRPs.

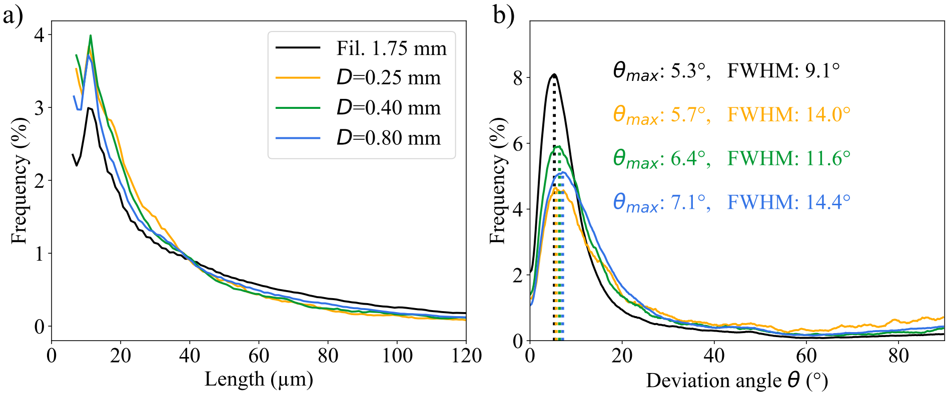

Figure 7: Probability density functions (PDFs) of a) fiber lengths and b) fiber deviation angles relative to printing direction (θ), for each nozzle diameter D. In a), the comparison to the PDF in the feedstock filament ($\varnothing$=1.75 mm) shows that fiber breakage occurs for all nozzle diameters to roughly the same degree. The peak locations (θ_{max}) on each curve and the full width at half maximum (FWHM) in b) reveal the effect of extrusion on fiber alignment. The drops in peak heights in b) could be explained by fiber breakage: the short segments produced by breaks are more likely to be misaligned. This effect is particularly prevalent in the 0.25 mm nozzle.

4.3. Local property variation

The same cumulative sum procedure described in Section 3.3.3 was used to visually analyze the microstructure for each printed configuration. As presented in the Video in Supplementary Materials, in addition to computing the cumulative sum of pixels containing fibers or pores, here each pixel is also given the value of a property: first fiber length, then fiber alignment with the 0° print direction. As a reminder, x and y are the 0° and 90° printing direction, respectively, the $x-y$ plane is the printing bed plane, and z is the vertical direction. Cumulative sums are taken along both x and y, enabling the study of gradients in material property, that is not easily seen on a slice-by-slice basis.

Figure 8 presents the cumulative sums of fiber alignment with the 0° print direction, fiber length, fiber and pore densities, for specimens printed with nozzle $D = 0.4$ mm, and the 0°-0° printing pattern. Three whole layers are visible, and one partially at the bottom. In Figure 8 a), we can see that there are pockets of stronger and weaker alignment (pale blue patches) that are of a size comparable to the layer height. This degree of non-uniformity is one possible explanation to the variability observed in tensile properties:

these variations are not always present depending on which specimen or scan location is considered. If more patches of weak alignment are present in a specimen, it would lead to lower macroscopic modulus in that direction. In addition, there is noticeable decrease in both fiber length and fiber density at the layer interfaces (Figure 8 b anc c). This effect is subtle, but indicative that different rheological characteristics are found at the interface. In Figure 8 d), we also observe a vertical gradient in the distribution of intra-bead porosity, which accumulate towards the bottom of each layer. These phenomena offers an interpretation to the known deviation of tensile and fracture properties at the inter-layer region.

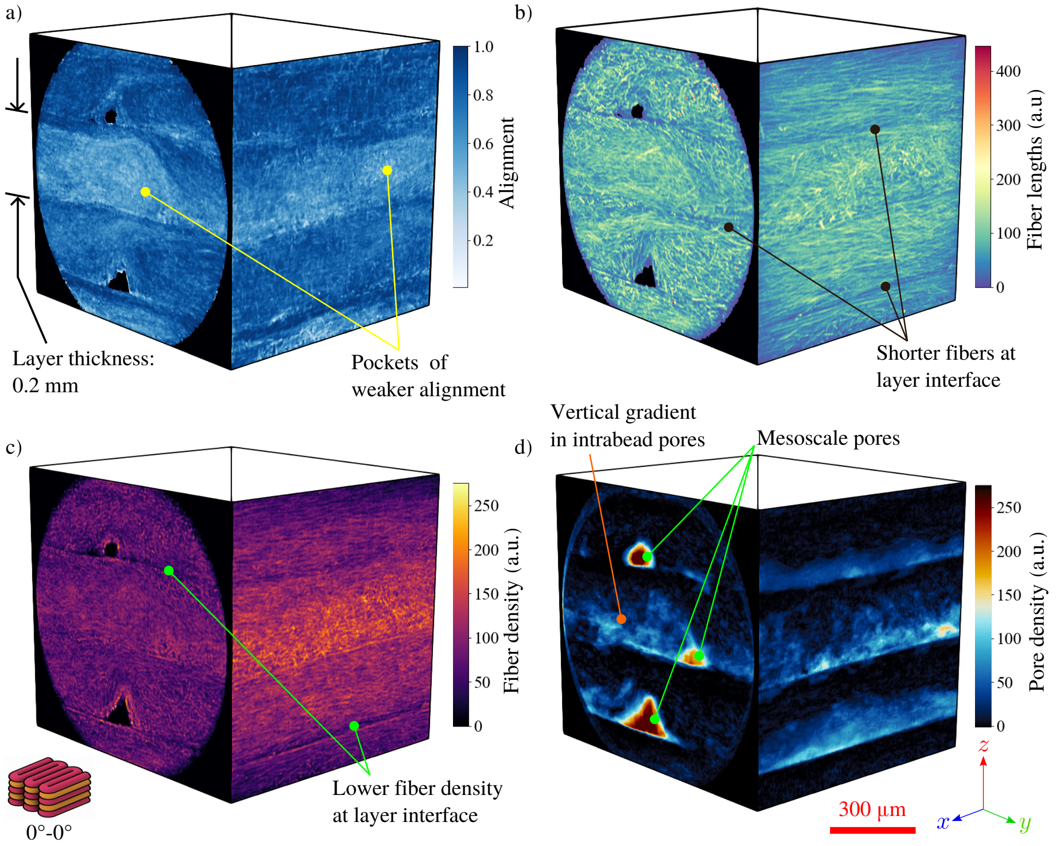

Figure 8: Morphology visualization: 0°-0° pattern, nozzle diameter $D = 0.4$ mm. Cumulative sum of per-voxel properties along x and y directions. a) Alignment with 0° print direction x (1.0 is perfect alignment ($\theta = 0°$), 0.0 is perpendicular ($\theta = 90°$)). b) Length of fibers. c) Fiber density. d) Pore density.

Figure 9 depicts the same cumulative sums, for specimens of nozzle $D = 0.4$ mm, and the 0°-90° printing pattern. From top to bottom, 4 layers are distinguished, namely 0°-90°-0°-90°. The alignment color code in Figure 9 a) is with direction x, therefore the white parts in the 90° layers are those with the strongest alignment with y. Again, regions of weaker alignment are perceptible in both the 0° and 90° passes, although in this case they are in the shape of elongated streaks. In addition, the $x - z$ (left-hand side) and $y - z$ (right-hand side) cumulative sums plots are not mirror images: the right-hand side shows much more pronounced waves. There are also noticeably longer fibers present in the center of those deeper indentations, as visible in Figure 9 b). We surmise this is due to the different cooling duration between the 0° pass and the 90° pass:

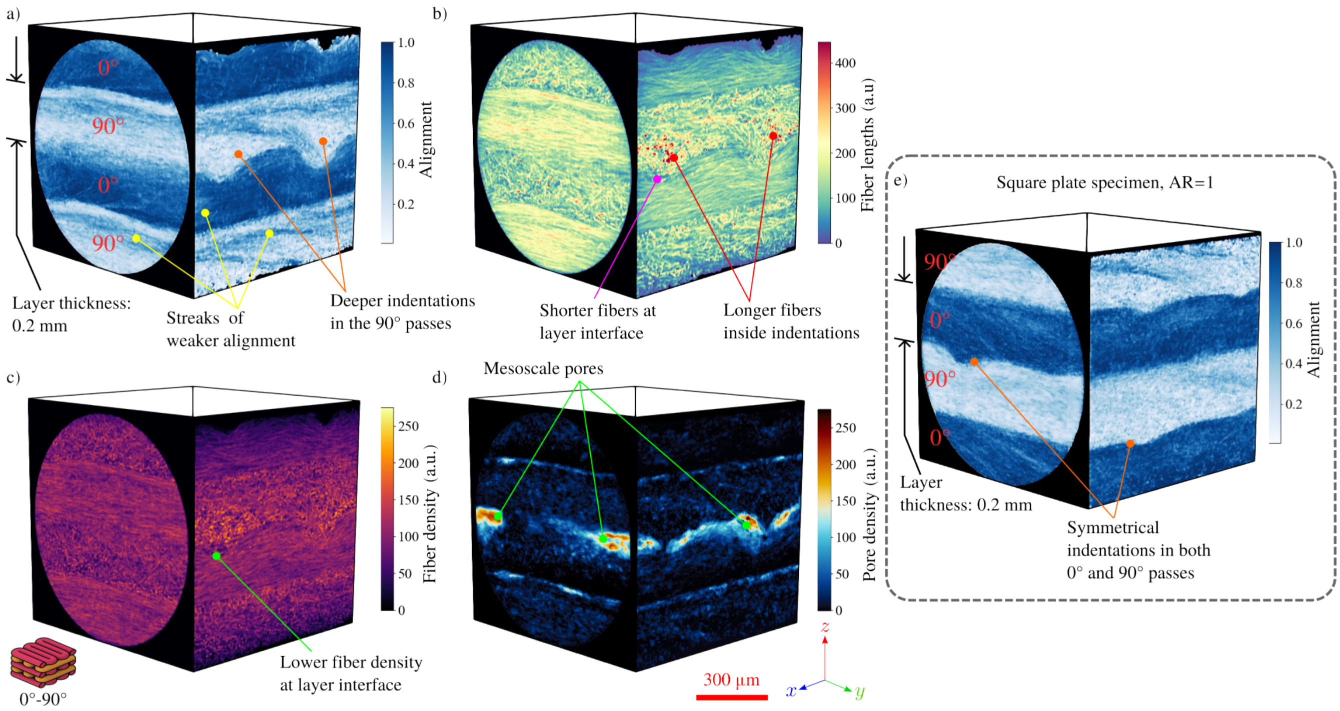

Figure 9: Morphology visualization: 0°-90° pattern, nozzle diameter $D = 0.4$ mm. Cumulative sum of per-voxel properties along x and y directions. a) Alignment with 0° print direction x (1.0 is perfect alignment ($\theta = 0°$), 0.0 is perpendicular ($\theta = 90°$)). b) Length of fibers. c) Fiber density. d) Pore density. e) Fiber alignment, using alternative square-shaped specimen (part aspect ratio of 1, dimensions $20 \times 20 \times 4$ mm). The indentations left on previous layers are of similar extent for print passes in both directions.

the central part of the dogbone specimen has a long aspect ratio. Therefore, the print head travels 115 mm for the 0° pass and only 6 mm for the 90° pass, a difference of 19 times. As a consequence, for each 90° bead much less cooling has occurred when the adjacent one is applied, therefore local base layer temperature is higher. More remelting of the base layer can thus occur, forming deeper indentations. We corroborate this explanation by scanning and analyzing a specimen made from a square plate (aspect ratio of 1, dimensions $20 \times 20 \times 4$ mm) printed in the 0°-90° configuration, also with the $D = 0.4$ mm nozzle. In Figure 9 e), the resulting cumulative sum visualization for fiber alignment in such a specimen is presented. In this scenario, the indentations left on the preceding layer are of similar severity for the passes in both directions. This effect suggests that feature aspect ratio is a source of microstructure orthotropy: the fiber alignment and length distribution is less symmetrical when part aspect ratio is high, leading to a different moduli in the x, y and z directions.

The reader is referred to the Supplementary Materials for the renderings of data from the nozzles with $D = 0.25$ mm and $D = 0.8$ mm mm. All these local variations highlight the need for using several FoVs across many specimens, as this is the only way to reach a true RVE for each printing configuration for this class of material.

4.4. Microscale orthotropy

It is expected that the presence of fibers in SFRP introduces transverse isotropy, i.e. the material's stiffness is symmetric with respect to rotation along one axis, here the printing direction x. However, the degree to which the microstructure by itself is orthotropic rather than transversely isotropic is not clear, meaning that the tensile moduli along directions y and z are also different from each other, which breaks the rotational symmetry along x. This effect is hard to disentangle from global orthotropy, to which the mesoscale printing pattern is a known contributor [13, 23–25]. Having a detailed description of the microstructure allows us to investigate this feature. As shown in Figure 10, each fiber in a microstructure can be represented in polar coordinates, in the following manner. The angle θ the fiber makes with the printing direction x is the radial coordinate, and the azimuthal angle in the $y - z$ plane is the angular coordinate. Doing so, a two-dimensional histogram can be generated, by binning all the fibers in a specimen by θ and ϕ. In addition, just as in artificial microstructure generation, the histogram is weighted to account for longer fibers' estimated effect on effective stiffness (see Section 3.5). Figure 11 presents the resulting histograms for nozzles with $D = 0.25$, 0.4 and 0.8 mm. The degree of alignment with print direction is higher for nozzle $D = 0.25$ and 0.8 mm, as seen in Figure 11 a) and c). The cumulative distribution function in Figure 11 d) shows that, for those specimen categories, 56% of all fibers have $\theta < 15°$, whereas for the $D = 0.4$ mm specimen the proportion is 29%. This explains the drop in tensile modulus observed in experiments, as presented in Table 3, where the $D = 0.4$ mm specimen is 14% less stiff in the x direction that the average of the $D = 0.25$ and 0.8 mm specimens. Furthermore, the more elongated and horizontally aligned red regions in Figure 11 b) indicate that the $D = 0.4$ mm specimen has a higher ratio of fibers aligned with the y direction against the z direction. This is not correlated with the extrusion cross-section (layer height/extrusion width, see Table 1), as the $D = 0.25$ and 0.4 mm specimen have a cross-section aspect ratio of 2, and the $D = 0.8$ mm specimen has an aspect ratio of 3. Nonetheless, this phenomenon deserves further investigation, as $D = 0.4$ mm nozzle offers a good trade-off between geometric print resolution and printing speed, but the drop in tensile properties is deleterious. Whereas the experimental measurement of microscale orthotropy, separately from the mesoscale contribution is not feasible, the degree of orthotropy can be gauged from the homogenized stiffness tensors at the microscale, $\tilde{\mathbf{C}}_{\text{micro}}$. The degree of congruence with either transverse isotropy or orthotropy can be measured by projecting $\tilde{\mathbf{C}}_{\text{micro}}$ to either space, i.e. rebuilding the tensor from the extracted independent parameters for each symmetry class, and measuring the $L2$ norm of the difference between the two. For instance the distance e of the projection into orthotropic space is: $e = \left|\tilde{\mathbf{C}}_{\text{micro}} - \tilde{\mathbf{C}}_{\text{micro}}^{\text{ortho}}\right|_{L2}$. The distances for all nozzle diameters are presented in Table 4, along with the ratio of tensile moduli along each of the reference directions. While the distance for the the $D = 0.25$

Table 4
Remainder of $\tilde{\mathbf{C}}_{\text{micro}}$ after projection to transversely isotropic and orthotropic space. Ratios of tensile moduli along x, y and z.

D, nozzle diameter (mm)	Printing pattern	Distance Trans. iso	Distance Orthotropy	E_z/E_y	E_z/E_x	E_y/E_x
0.25	$0° - 0°$	1.15	1.07	0.97	0.26	0.27
0.40	$0° - 0°$	3.02	1.86	0.84	0.33	0.40
0.80	$0° - 0°$	2.08	2.02	0.96	0.24	0.25
0.40	$0° - 90°$	8.88	1.71	0.42	0.63	1.52
0.40 (plate)	$0° - 90°$	5.53	0.70	0.52	0.54	1.04
0.40	$90° - 90°$	1.26	1.19	1.02	0.25	0.24

and 0.8 mm specimens are nearly identical for both symmetry classes, the one for the $D = 0.4$ mm specimen has a value 50% larger for transverse isotropy than orthotropy. The same effect is noticeable with the E_z/E_y which is further from unit for the latter specimen, and the moduli perpendicular to the printing direction E_z/E_x and E_y/E_x are also relatively larger.

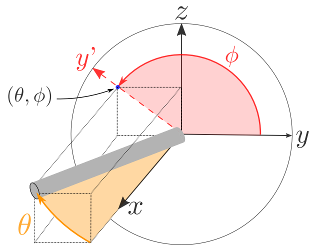

Figure 10: Polar representation of a fiber by its deviation angle θ and azimuthal angle ϕ. The angle θ the fiber makes with the printing direction x becomes the radial coordinate, and the angular coordinate ϕ is the angle made by the $x - y'$ plane containing the fiber and the $x - y$ print bed plane.

However, in many applications, having an isotropic response is preferable, for which the 0°-90° printing pattern is better suited. In Figure 12, the histograms for the $D = 0.4$ mm nozzle are presented, first by separating the fibers in the 0° and the 90° passes in Figures 12 a) and b), then by showing both passes together in Figure 12 c). Note that the 90° pass is made in the y direction, therefore most fibers in that pass have values of $\theta \sim 90$ and $\phi \sim 0, 180$, where the two red regions in Figure 12 b) are located. However, much as was observed in the morphological visualizations in Figure 9, the two directions show salient asymmetry. As can be observed visually, no red region is present in Figure 12 a), meaning the concentration of fibers aligned with x is lower. In addition, the ratio of fibers better aligned with y to those aligned with x is 57:43, suggesting the different thermal conditions seen by the 90° pass are more favorable to fiber alignment in that direction. The difference in alignment between the two passes suggests tensile properties are inferior in the x direction (0°) than the y direction (90°), likely due to part aspect ratio. That prediction is corroborated in the homogenization output, as seen in Table 4: just as the alignment profile was asymetrical in the dogbone

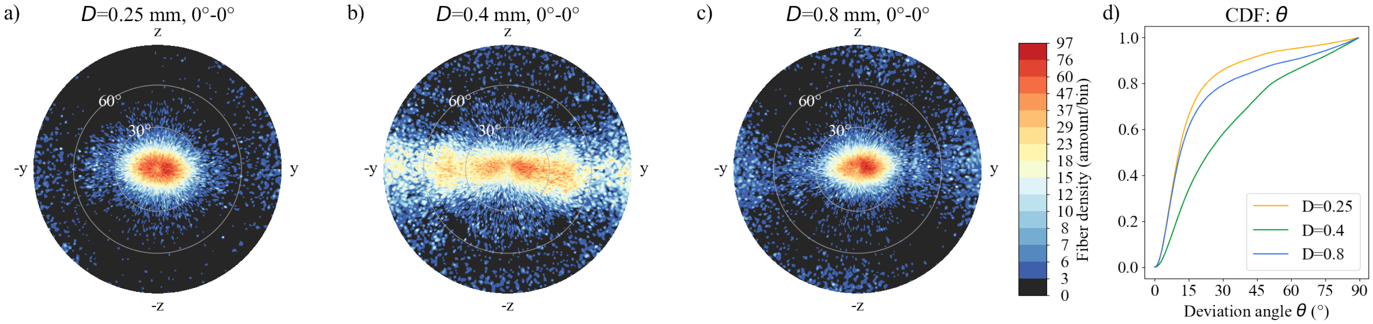

Figure 11: Histogram of fibers angular distributions, for the 0°-0° specimen made with: a) nozzles $D = 0.25$ mm, b) $D = 0.4$ mm and c) $D = 0.8$ mm, including $\sim 10^5$ individual fibers each. The radial coordinate is the deviation angle θ, and the angular coordinate is the azimuthal angle ϕ. As the cumulative distribution function of θ for each nozzle diameter showns in d), the specimens made with 0.25 and 0.8 mm nozzles have their fibers much more aligned with the print direction, with 56% of fibers with $\theta < 15°$, when compared to 29% for the $D = 0.4$ mm nozzle, which explains lower axial tensile properties for the latter. In addition, the specimen made with $D = 0.4$ mm nozzle exhibits a preferential alignment in the y direction (ratio between y-alignment and z-alignment of 74:26 instead of 61:39 for $D = 0.25$ and 0.8 mm).

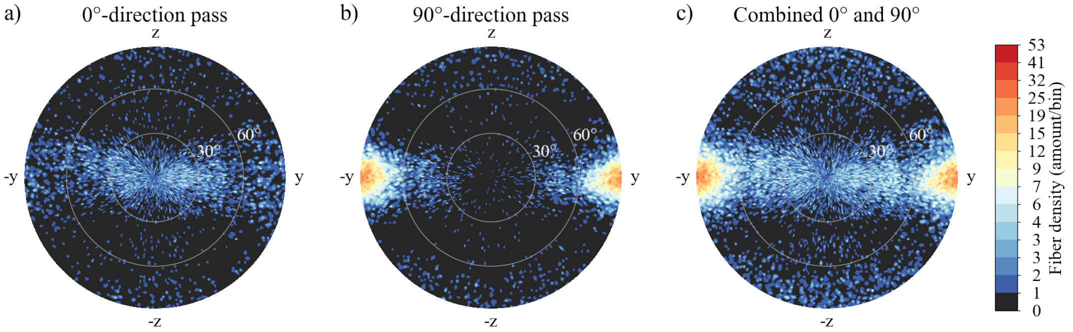

Figure 12: Histogram of fibers angular distributions, for the 0°-90° specimen made with the $D = 0.4$ mm nozzle. The fibers are separated as belonging to: a) the 0° pass, b) the 90° pass, and c) both 0° and 90° passes combined. More fibers are aligned with the y direction than with the x direction, with a ratio of 53:47, introducing orthotropy, attributable to part aspect ratio of 19 in ASTM D638 Type 4 dogbones.

specimen vs. the square plate, the $\tilde{\mathbf{C}}_{\text{micro}}$ is also far more symmetrical for the plate specimen, with a ratio of E_y/E_x=1.04, against 1.52 in the dogbone specimen.

4.5. FFT Homogenization results

Using the fully detailed description of the microstructure for elastic homogenization allows the study of the stress-strain fields that develop inside the material. In Figure 13, a slice oriented in the printing bed plane inside one of the subvolumes used for homogenization for a specimen printed with the 0°-0° pattern and the $D = 0.25$ mm nozzle is presented. For this nozzle, the micro and mesoscale homogenization are made in a single step as the printing pattern is present at a length scale close that of the individual fibers. In Figure 13 a), the tomographic data is depicted, where the fibers are distinguished in white, the matrix in grey, and the pores in dark. The printing pattern is also discernible, with the extrusion width annotated in red. In Figure 13 b) and c), the von Mises strain and stress fields computed with the help of AMITEX

Table 5
FFT-simulation results, microscale only ($\tilde{\mathbf{C}}_{\text{micro}}$)

D, **nozzle diameter**	**Pattern**	E_x (GPa)	E_y (GPa)	E_z (GPa)
0.25	$0° - 0°$	20.30	5.53	5.37
0.40	$0° - 0°$	18.32	7.27	6.13
0.80	$0° - 0°$	21.37	5.30	5.10
0.40	$0° - 90°$	10.07	15.26	6.34
0.40 (plate)	$0° - 90°$	11.25	11.75	6.07
0.40	$90° - 90°$	5.59	23.21	5.73

are presented. The fibers being the phase with the highest stiffness, most of the stress concentrates inside them, and they exhibit very little strain. The opposite is true for the pores: they have no stiffness, therefore they develop no stress, and the maximum values of strain are inside them, as they deform freely (contrary to what is done in the FE method, in FFT-homogenization the nodes are regularly-spaced, meaning the inside of pores is also solved for).Inside the matrix phase, we can observe stress concentration near the tip of fibers, or where pores have sharp corners. Those locations are likely to be damage initiation sites.

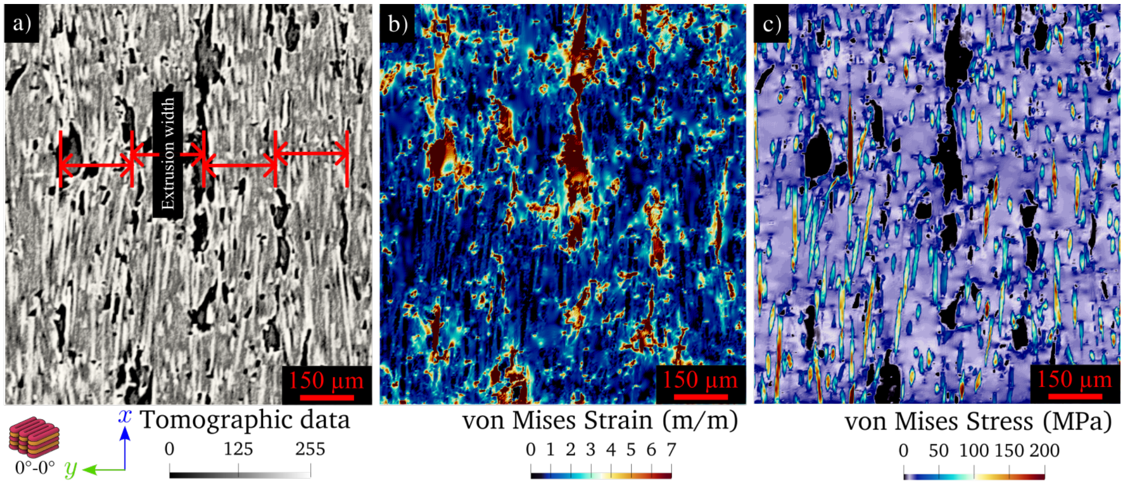

Figure 13: Result of the FFT homogenization procedure on a subvolume of a specimen made with the $D = 0.25$ mm nozzle and the 0°-0° printing pattern. a) Tomographic data in the plane of the printing bed. b) Von Mises strain field, mainly present in pores. c) Von Mises stress field, concentrating inside fibers.

In Figure 14, the mesoscale homogenization results for the specimen made with the 0°-0° printing pattern and the $D = 0.4$ mm nozzle are presented. In this case, only two phases are homogenized: the mesoscale porosity and the solid phase described by the $\tilde{\mathbf{C}}_{\text{micro}}$ stiffness tensor obtained at the microscale homogenization step. In Figure 14 b), the strain field is again maximal inside pores, however the strain also forms bands in the vertical direction. In Figure 14 c), the stress field shows that stress concentrates where the mesoscale pores form small radii.

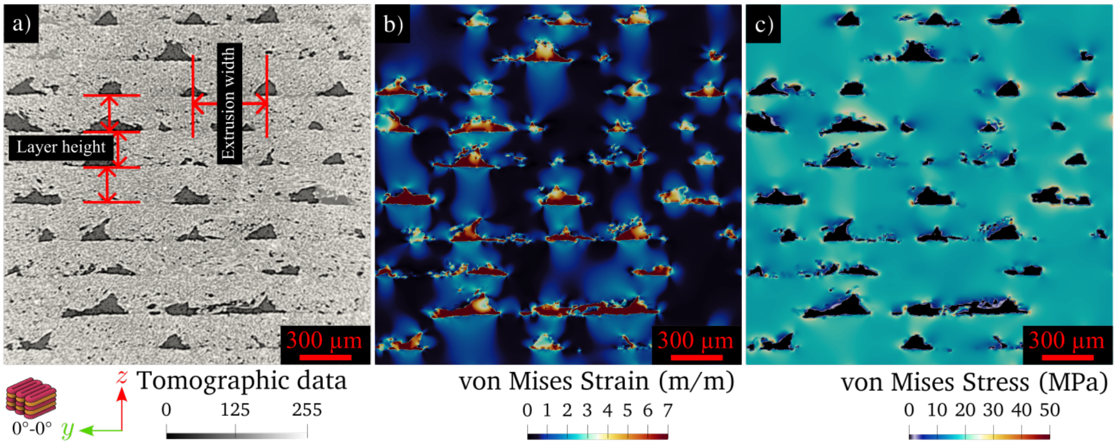

Figure 14: Resulting stress-strain fields for the mesoscale FFT homogenization procedure on a subvolume of a specimen made with the $D = 0.4$ mm nozzle and the 0°-0° printing pattern (0° is out-of-plane). a) Tomographic data. b) Von Mises strain field. c) Von Mises stress field.

Table 6
FFT-simulation results, dual-scale homogenization ($\tilde{\mathbf{C}}_{\text{meso}}$). For the $D = 0.25$ mm nozzle, both the separate and simultaneous dual-scale outputs are shown.

D, nozzle diameter (mm)	Pattern	E_x (GPa)	E_y (GPa)	E_z (GPa)	Experimental E_x (GPa)	Relative error (%)
0.25 (simultaneous)	$0° - 0°$	18.76	5.02	4.60	19.4 ± 1.0	3.37
0.25 (separate)	$0° - 0°$	17.67	4.64	4.17	19.4 ± 0.7	8.98
0.40	$0° - 0°$	15.60	5.69	3.49	16.4 ± 0.7	4.60
0.80	$0° - 0°$	18.82	4.63	4.31	18.5 ± 1.0	1.63
0.40	$0° - 90°$	8.80	13.30	4.25	9.7 ± 0.6	9.63
0.40	$90° - 90°$	4.37	19.55	3.23	3.2 ± 0.3	36.23

4.6. Simulation vs experimental results

In Tables 5 and 6, the homogenization results for each specimen type are presented, for the microscale and the mesoscale, respectively. The relative errors between the tensile testing values and the prediction for FFT-homogenization using real data are all below 5%, except for the 90°-90° specimen with the 0.4 mm nozzle which has a 36% error. For the $D = 0.25$ mm nozzle, the relevance of using simultaneous dual-scale instead of separating them as for the rest of the specimen types is demonstrated: the relative error is nearly halved by doing simultaneous dual-scale homogenization, as the scale separation is insufficient in this case to successfully account for $\tilde{\mathbf{C}}_{\text{micro}}$ alone.

In Figure 15, the final output of the dual-scale FFT-homogenization procedure for each specimen type is presented, along with the tensile testing measurements, and the results of the alternate method using artificial microstructures for the microscale step. The confidence intervals in the simulated results are calculated from the dispersion of results for each subvolumes in each of the simulated cases. The relative errors between the tensile testing values and the predictions made with artificial data are all in excess of 19%. Even though the artificial microstructures used are simplified, the recourse to fully detailed mesostructures makes the prediction quality somewhat improved, when compared to similar methods in the literature [2, 22]. Nonetheless, using real microstructures is considerably more reliable, and the prediction quality is within or near the confidence interval for the experimental measurements. A few sources of error that affect the result quality bear mentioning. First, the material variability due to the manufacturing process is considerable, as witnessed by the width of the confidence intervals in tensile properties themselves. Then, local morphological properties can vary within and between specimens, which affects both physical specimens as well as homogenization prediction quality. Then, the FFT method assumes periodic boundary conditions. When generating artificial microstructures, both RSA or molecular dynamics methods enforce geometrical periodicity by repeating fiber segments that exceed the unit-cell boundary on the opposite side, which isn't the case in microstructures based on real (non-periodic) imaging data. Also, the matrix-fiber interface is considered ideal in our method, which is likely not true in real materials [26], and were this included, the homogenization prediction would be somewhat lower. However, the quality of these results for such a broad range of morphological configurations leaves no doubt that using rich microstructures from actual specimen is a decisive advantage over relying on artificial geometries. Note that the simplification made in some studies considering isotropic CFs [2] is not advisable: when our simulations were done with isotropic CFs, the estimated moduli were in excess of 20% above experiment. Using transversely isotropic CFs, while requiring more analysis to differentiate individual fibers, is also a determining factor for successful homogenization. In addition, the number of fibers that encompass the RVEs are in the order of 10^4, much higher than the customary $10 - 200$. Each of the predictions in Figure 15 requires $\approx$ 10 h in combined processing on AMITEX, using 24 CPUs and 90GB of RAM. This is on top of the $\approx$ 20 h of extraction done on OpenFiberSeg for each FoV.

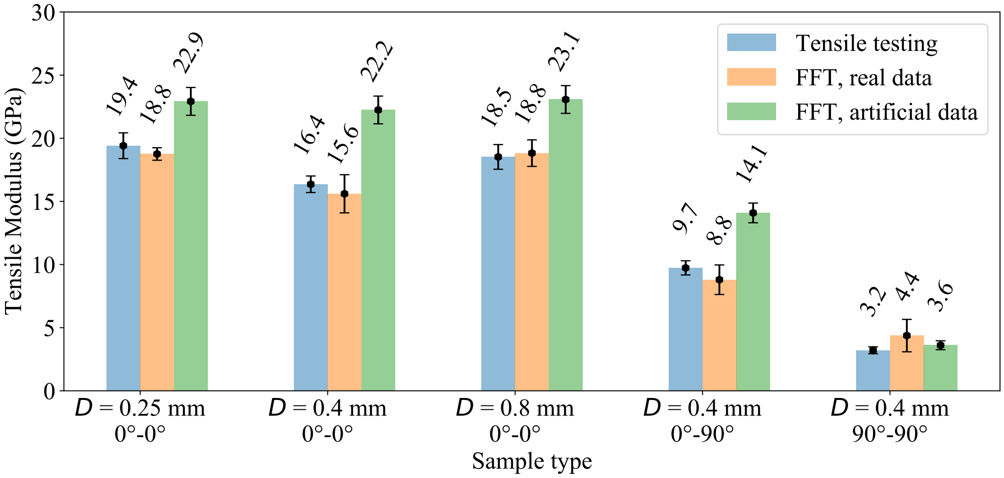

Figure 15: Comparison of tensile moduli as predicted from FFT-homogenization and as measured experimentally. Values are averaged for at least 4 subvolumes in each configuration. The error bars indicate 95% confidence intervals. The variation in the simulation output is representative of the spread of values encountered for the subvolumes that makeup the RVE for each configuration.

5. Conclusion

In this work, the process-structure-property relation for FFF SFRPs is investigated, including the effect of using three nozzle diameters, and three different printing patterns. Physical specimens were produced and comprehensively characterized, using μCT imaging and individual component extraction, both in free-space extrusion (no contact with print bed) or in standard tensile testing specimen. Dual-scale homogenization was employed to successfully predict the tensile properties of 5 different print configurations, and it was demonstrated that the relative errors are reduced by a factor of 4, when compared to using simplified artificial microstructure descriptions. Variations in local morphology and in angular deviations between specimens were exposed, which provides insight into the variability in tensile properties between specimen. For instance, the large angular dispersion in specimens made with a $D = 0.4$ mm nozzle explain the lower tensile moduli. In addition, the impact of part aspect ratio on the microscopic morphology is revealed, which is an important phenomena for predicting part behavior for real applications. Future work on this topic would include a more rigorous handling of the size of representative volume element (RVE), an exploration of inter-layer properties, the application of this method to fracture modelling, the use of imperfect matrix-fiber interfaces, and mechanical modelling using parts of more complex geometry, infill pattern and loading scenarios. The FFT homogenization method can also be applied to FFF SFRPs to study other material behavior laws, including thermal and electrical conductivity, thermal expansion, viscoelasticity and piezoelectricity.

6. Source code and data repository

The full source code repository and selected original tomographic data including processed results are available at `https://github.com/lm2-poly/OpenFiberSeg`.

Acknowledgements

This project was supported financially and conducted with the technical and financial support of Safran S.A. (FACMO Research Chair). Financial support was also granted by the Natural Sciences and Engineering Research Council of Canada (Alexander Graham Bell Canada Graduate Scholarship program, and the Collaborative Research and Development program, grant no CRDPJ514761). Further funding was obtained through the Simulation-based Engineering Science program funded through the CREATE program. High performance computing ressources were made available by Calcul Québec (`calculquebec.ca`) and the Digital Research Alliance of Canada (`alliancecan.ca`).

References

[1] P. Parandoush, D. Lin, A review on additive manufacturing of polymer-fiber composites, Composite Structures 182 (2017) 36–53.

[2] A. Nasirov, A. Gupta, S. Hasanov, I. Fidan, Three-scale asymptotic homogenization of short fiber reinforced additively manufactured polymer composites, Composites Part B: Engineering 202 (2020) 108269.

[3] B. Brenken, E. Barocio, A. Favaloro, V. Kunc, R. B. Pipes, Fused filament fabrication of fiber-reinforced polymers: A review, Additive Manufacturing 21 (2018) 1–16.

[4] P. Wang, B. Zou, H. Xiao, S. Ding, C. Huang, Effects of printing parameters of fused deposition modeling on mechanical properties, surface quality, and microstructure of peek, Journal of Materials Processing Technology 271 (2019) 62–74.

[5] M. Rinaldi, F. Cecchini, L. Pigliaru, T. Ghidini, F. Lumaca, F. Nanni, Additive manufacturing of polyether ether ketone (peek) for space applications: A nanosat polymeric structure, Polymers 13 (2021) 11.

[6] J. P. Lewicki, J. N. Rodriguez, C. Zhu, M. A. Worsley, A. S. Wu, Y. Kanarska, J. D. Horn, E. B. Duoss, J. M. Ortega, W. Elmer, et al., 3d-printing of meso-structurally ordered carbon fiber/polymer composites with unprecedented orthotropic physical properties, Scientific reports 7 (2017) 1–14.

[7] X. Liu, V. Shapiro, Homogenization of material properties in additively manufactured structures, Computer-Aided Design 78 (2016) 71–82.

[8] T. Baranowski, D. Dobrovolskij, K. Dremel, A. Hölzing, G. Lohfink, K. Schladitz, S. Zabler, Local fiber orientation from x-ray region-of-interest computed tomography of large fiber reinforced composite components, Composites Science and Technology 183 (2019) 107786.

[9] H. Tang, H. Chen, Q. Sun, Z. Chen, W. Yan, Experimental and computational analysis of structure-property relationship in carbon fiber reinforced polymer composites fabricated by selective laser sintering, Composites Part B: Engineering 204 (2021) 108499.

[10] H. Zhang, L. Zhang, H. Zhang, J. Wu, X. An, D. Yang, Fibre bridging and nozzle clogging in 3d printing of discontinuous carbon fibre-reinforced polymer composites: Coupled cfd-dem modelling, The International Journal of Advanced Manufacturing Technology 117 (2021) 3549–3562.

[11] F.-L. Guo, J.-M. Hu, T. Guan, Y.-T. Fu, C.-Y. Huang, Y.-Q. Li, S.-Y. Fu, Modeling and characterizations of mechanical behaviors of short carbon fiber and short glass fiber reinforced polyetherimide composites, Composites Science and Technology (2022) 109685.

[12] H. L. Tekinalp, V. Kunc, G. M. Velez-Garcia, C. E. Duty, L. J. Love, A. K. Naskar, C. A. Blue, S. Ozcan, Highly oriented carbon fiber–polymer composites via additive manufacturing, Composites Science and Technology 105 (2014) 144–150.

[13] P. Biswas, S. Guessasma, J. Li, Numerical prediction of orthotropic elastic properties of 3d-printed materials using micro-ct and representative volume element, Acta Mechanica 231 (2020) 503–516.

[14] W. Tian, L. Qi, J. Zhou, J. Liang, Y. Ma, Representative volume element for composites reinforced by spatially randomly distributed discontinuous fibers and its applications, Composite Structures 131 (2015) 366–373.

[15] P. Feraboli, T. Cleveland, P. Stickler, J. Halpin, Stochastic laminate analogy for simulating the variability in modulus of discontinuous composite materials, Composites Part A: Applied Science and Manufacturing 41 (2010) 557–570.

[16] K. Wang, S. Pei, Y. Li, J. Li, D. Zeng, X. Su, X. Xiao, N. Chen, In-situ 3d fracture propagation of short carbon fiber reinforced polymer composites, Composites Science and Technology 182 (2019) 107788.

[17] E. Bertevas, J. Férec, B. C. Khoo, G. Ausias, N. Phan-Thien, Smoothed particle hydrodynamics (sph) modeling of fiber orientation in a 3d printing process, Physics of Fluids 30 (2018) 103103.

[18] V. Müller, M. Kabel, H. Andrä, T. Böhlke, Homogenization of linear elastic properties of short-fiber reinforced composites–a comparison of mean field and voxel-based methods, International Journal of Solids and Structures 67 (2015) 56–70.

[19] P. A. Hessman, T. Riedel, F. Welschinger, K. Hornberger, T. Böhlke, Microstructural analysis of short glass fiber reinforced thermoplastics based on x-ray micro-computed tomography, Composites Science and Technology 183 (2019) 107752.

[20] C. Gierden, J. Kochmann, J. Waimann, B. Svendsen, S. Reese, A review of fe-fft-based two-scale methods for computational modeling of microstructure evolution and macroscopic material behavior, Archives of Computational Methods in Engineering (2022) 1–21.

[21] A. Nasirov, I. Fidan, Prediction of mechanical properties of fused filament fabricated structures via asymptotic homogenization, Mechanics of Materials 145 (2020) 103372.

[22] A. Gupta, S. Hasanov, I. Fidan, Z. Zhang, Homogenized modeling approach for effective property prediction of 3d-printed short fibers reinforced polymer matrix composite material, The International Journal of Advanced Manufacturing Technology (2021) 1–18.

[23] A. Bellini, S. Güçeri, Mechanical characterization of parts fabricated using fused deposition modeling, Rapid Prototyping Journal (2003).

[24] M. Domingo-Espin, J. M. Puigoriol-Forcada, A.-A. Garcia-Granada, J. Llumà, S. Borros, G. Reyes, Mechanical property characterization and simulation of fused deposition modeling polycarbonate parts, Materials & Design 83 (2015) 670–677.

[25] S. Dai, Z. C. Deng, Y. J. Yu, K. Zhang, S. H. Wang, J. Ye, Orthotropic elastic behaviors and yield strength of fused deposition modeling materials: Theory and experiments, Polymer Testing 87 (2020) 106520.

[26] Y. Abderrafai, M. H. Mahdavi, F. Sosa-Rey, C. Hérard, I. O. Navas, N. Piccirelli, M. Lévesque, D. Therriault, Additive manufacturing of short carbon fiber-reinforced polyamide composites by fused filament fabrication: Formulation, manufacturing and characterization, Materials & Design 214 (2022) 110358.

[27] I. Hanhan, R. Agyei, X. Xiao, M. D. Sangid, Comparing non-destructive 3d x-ray computed tomography with destructive optical microscopy for microstructural characterization of fiber reinforced composites, Composites Science and Technology 184 (2019) 107843.

[28] A. Bernasconi, F. Cosmi, P. Hine, Analysis of fibre orientation distribution in short fibre reinforced polymers: A comparison between optical and tomographic methods, Composites Science and Technology 72 (2012) 2002–2008.

[29] F. Sosa-Rey, Y. Abderrafai, A. D. Lewis, D. Therriault, N. Piccirelli, M. Lévesque, Openfiberseg: Open-source segmentation of individual fibers and porosity in tomographic scans of additively manufactured short fiber reinforced composites, Composites Science and Technology (2022) 109497.

[30] V. Müller, B. Brylka, F. Dillenberger, R. Glöckner, S. Kolling, T. Böhlke, Homogenization of elastic properties of short-fiber reinforced composites based on measured microstructure data, Journal of Composite Materials 50 (2016) 297–312.

[31] N. Davidson, A. Clarke, G. Archenhold, Large-area, high-resolution image analysis of composite materials, Journal of Microscopy 185 (1997) 233–242.

[32] C. Eberhardt, A. Clarke, Fibre-orientation measurements in short-glass-fibre composites. part i: automated, high-angular-resolution measurement by confocal microscopy, Composites Science and Technology 61 (2001) 1389–1400.

[33] Z. Wang, D. E. Smith, D. A. Jack, A statistical homogenization approach for incorporating fiber aspect ratio distribution in large area polymer composite deposition additive manufacturing property predictions, Additive Manufacturing 43 (2021) 102006.

[34] T. Mishurova, N. Rachmatulin, P. Fontana, T. Oesch, G. Bruno, E. Radi, I. Sevostianov, Evaluation of the probability density of inhomogeneous fiber orientations by computed tomography and its application to the calculation of the effective properties of a fiber-reinforced composite, International Journal of Engineering Science 122 (2018) 14–29.

[35] E. Ghossein, Numerical Validation of Analytical Homogenization Models for the Case of Randomly Distributed and Oriented Ellipsoidal Fibers Reinforced Composites, Ph.D. thesis, École polytechnique de Montréal, 2014.

[36] E. Ghossein, M. Lévesque, Homogenization models for predicting local field statistics in ellipsoidal particles reinforced composites: Comparisons and validations, International Journal of Solids and Structures 58 (2015) 91–105.

[37] C. Suarez-Afanador, R. Cornaggia, N. Lahellec, A. Maurel-Pantel, D. Boussaa, H. Moulinec, S. P.-A. Bordas, Effective thermo-viscoelastic behavior of short fiber reinforced thermo-rheologically simple polymers: An application to high temperature fiber reinforced additive manufacturing, European Journal of Mechanics-A/Solids (2022) 104701.

[38] L. Chen, B. Gu, J. Zhou, J. Tao, Study of the effectiveness of the rves for random short fiber reinforced elastomer composites, Fibers and Polymers 20 (2019) 1467–1479.

[39] T. Kanit, S. Forest, I. Galliet, V. Mounoury, D. Jeulin, Determination of the size of the representative volume element for random composites: statistical and numerical approach, International Journal of solids and structures 40 (2003) 3647–3679.

[40] J. Dirrenberger, S. Forest, D. Jeulin, Towards gigantic rve sizes for 3d stochastic fibrous networks, International Journal of Solids and Structures 51 (2014) 359–376.

[41] E. Ghossein, M. Lévesque, Random generation of periodic hard ellipsoids based on molecular dynamics: A computationally-efficient algorithm, Journal of Computational Physics 253 (2013) 471–490.

[42] A. Diouf-Lewis, R. D. Farahani, F. Iervolino, J. Pierre, Y. Abderrafai, M. Lévesque, N. Piccirelli, D. Therriault, Design and characterization of carbon fiber-reinforced peek/pei blends for fused filament fabrication additive manufacturing, Materials Today Communications 31 (2022) 103445.

[43] J. Feder, Random sequential adsorption, Journal of Theoretical Biology 87 (1980) 237–254.

[44] J. Talbot, P. Schaaf, G. Tarjus, Random sequential addition of hard spheres, Molecular Physics 72 (1991) 1397–1406.

[45] L. Qi, W. Tian, J. Zhou, Numerical evaluation of effective elastic properties of composites reinforced by spatially randomly distributed short fibers with certain aspect ratio, Composite Structures 131 (2015) 843–851.

[46] B. D. Lubachevsky, F. H. Stillinger, Geometric properties of random disk packings, Journal of statistical Physics 60 (1990) 561–583.

[47] A. Donev, S. Torquato, F. H. Stillinger, Neighbor list collision-driven molecular dynamics simulation for nonspherical hard particles. i. algorithmic details, Journal of computational physics 202 (2005) 737–764.

[48] R. F. Agyei, M. D. Sangid, A supervised iterative approach to 3d microstructure reconstruction from acquired tomographic data of heterogeneous fibrous systems, Composite Structures 206 (2018) 234–246.

[49] M. W. Czabaj, M. L. Riccio, W. W. Whitacre, Numerical reconstruction of graphite/epoxy composite microstructure based on sub-micron resolution x-ray computed tomography, Composites Science and Technology 105 (2014) 174–182.

[50] P. J. Creveling, W. W. Whitacre, M. W. Czabaj, A fiber-segmentation algorithm for composites imaged using x-ray microtomography: Development and validation, Composites Part A: Applied Science and Manufacturing 126 (2019)

105606.

[51] M. Somireddy, A. Czekanski, Computational modeling of constitutive behaviour of 3d printed composite structures, Journal of Materials Research and Technology 11 (2021) 1710–1718.

[52] B. P. Heller, D. E. Smith, D. A. Jack, Effects of extrudate swell and nozzle geometry on fiber orientation in fused filament fabrication nozzle flow, Additive Manufacturing 12 (2016) 252–264.

[53] S. G. Advani, C. L. Tucker III, The use of tensors to describe and predict fiber orientation in short fiber composites, Journal of rheology 31 (1987) 751–784.

[54] J. M. Chacón, M. Á. Caminero, P. J. Núñez, E. García-Plaza, J. P. Bécar, Effect of nozzle diameter on mechanical and geometric performance of 3d printed carbon fibre-reinforced composites manufactured by fused filament fabrication, Rapid Prototyping Journal 27 (2021) 769–784.

[55] B. Hausnerova, N. Honkova, A. Lengalova, T. Kitano, P. Saha, Rheology and fiber degradation during shear flow of carbon-fiber-reinforced polypropylenes, Polymer Science Series A 48 (2006) 951–960.

[56] T. Mori, K. Tanaka, Average stress in matrix and average elastic energy of materials with misfitting inclusions, Acta metallurgica 21 (1973) 571–574.

[57] Y. Benveniste, A new approach to the application of mori-tanaka's theory in composite materials, Mechanics of materials 6 (1987) 147–157.

[58] R. Christensen, K. Lo, Solutions for effective shear properties in three phase sphere and cylinder models, Journal of the Mechanics and Physics of Solids 27 (1979) 315–330.

[59] G. Lielens, P. Pirotte, A. Couniot, F. Dupret, R. Keunings, Prediction of thermo-mechanical properties for compression moulded composites, Composites Part A: Applied Science and Manufacturing 29 (1998) 63–70.

[60] J. Spahn, H. Andrä, M. Kabel, R. Müller, A multiscale approach for modeling progressive damage of composite materials using fast fourier transforms, Computer Methods in Applied Mechanics and Engineering 268 (2014) 871–883.

[61] M. G. Pike, C. Oskay, Three-dimensional modeling of short fiber-reinforced composites with extended finite-element method, Journal of Engineering Mechanics 142 (2016) 04016087.

[62] H. Moulinec, P. Suquet, A numerical method for computing the overall response of nonlinear composites with complex microstructure, Computer methods in applied mechanics and engineering 157 (1998) 69–94.

[63] S. Lucarini, M. V. Upadhyay, J. Segurado, Fft based approaches in micromechanics: fundamentals, methods and applications, Modelling and Simulation in Materials Science and Engineering (2021).

[64] H. Moulinec, F. Silva, Comparison of three accelerated fft-based schemes for computing the mechanical response of composite materials, International Journal for Numerical Methods in Engineering 97 (2014) 960–985.

[65] L. Gélébart, J. Derouillat, Amitex_fftp website, 2020. URL: `https://amitexfftp.github.io/AMITEX/index.html`.

[66] L. Gélébart, R. Mondon-Cancel, Non-linear extension of fft-based methods accelerated by conjugate gradients to evaluate the mechanical behavior of composite materials, Computational Materials Science 77 (2013) 430–439.

[67] P. Bhattacharya, Q. Li, D. Lacroix, V. Kadirkamanathan, M. Viceconti, A systematic approach to the scale separation problem in the development of multiscale models, PloS one 16 (2021) e0251297.

[68] C. Boutin, J.-L. Auriault, C. Geindreau, Homogenization of coupled phenomena in heterogenous media, volume 149, John Wiley & Sons, 2010.

[69] Victrex peek 450g, 2022. URL: `https://www.victrex.com/-/media/downloads/datasheets/victrex_tds_450g.pdf?rev=daedb99925fe462ab1863cafb0f2c0aa`.

[70] What's the difference between t300 t700 and t800 carbon fiber?, 2020. URL: `https://www.jinjiuyi.net/news/difference-between-t300-t700-and-t800-carbon-fiber.html`.

[71] T300 datasheet, 2022. URL: `https://www.toraycma.com/wp-content/uploads/T300-Technical-Data-Sheet-1.pdf.pdf`.

[72] H. Miyagawa, T. Mase, C. Sato, E. Drown, L. T. Drzal, K. Ikegami, Comparison of experimental and theoretical transverse elastic modulus of carbon fibers, Carbon 44 (2006) 2002–2008.

[73] B. A. Lippmann, J. Schwinger, Variational principles for scattering processes. i, Physical Review 79 (1950) 469.

[74] T. Mura, Micromechanics of defects in solids, Springer Science & Business Media, 2013.

[75] D. J. Eyre, G. W. Milton, A fast numerical scheme for computing the response of composites using grid refinement, The European Physical Journal-Applied Physics 6 (1999) 41–47.

A. Appendix: Deriving effective properties of a microstructure

Notation and conventions used

In the following discussions, unless otherwise specified scalars are represented by lowercase letters (a, b, α, β), vectors by lowercase latin bold letters $(\mathbf{a},\mathbf{b})$, 2^{nd}-order tensors by lowercase bold greek letters: $(\boldsymbol{\varepsilon}, \boldsymbol{\sigma})$, 4^{th}-order tensors by uppercase bold Latin letters: $(\mathbf{C}, \mathbf{S})$. Einstein summation convention is adopted, which reads for the singly contracted product:

$$\mathbf{a} \cdot \mathbf{b} = a_i b_i = \sum_i a_i b_i = \ c \text{ (a scalar)} \tag{A.1}$$

$$\boldsymbol{\alpha} \cdot \boldsymbol{\beta} = \alpha_{ij}\beta_{jk} = \sum_j \alpha_{ij}\beta_{jk} = \ \delta_{ik} = \boldsymbol{\delta} \text{ (a } 2^{nd}\text{-order tensor)} \tag{A.2}$$

The doubly-contracted tensor product is denoted: $A_{ijkl}x_{jl} = b_{ik}$, or $\mathbf{A} : \mathbf{x} = \mathbf{b}$. The spatial averaging operation is denoted $\bar{b} = \langle b(\mathbf{x}) \rangle$ (with b being a scalar or tensor of any order).

The 4^{th} rank tensors that are of relevance to continuum mechanics generally present minor and major symmetries, and can be represented concisely in the so-called modified Voigt notation. A $4^{th}-$order tensor

$\boldsymbol{A}$ takes the following modified Voigt notation:

$$\boldsymbol{A}_{ijkl} = \begin{bmatrix} A_{1111} & A_{1122} & A_{1133} & \sqrt{2}A_{1123} & \sqrt{2}A_{1131} & \sqrt{2}A_{1112} \\ A_{2211} & A_{2222} & A_{2233} & \sqrt{2}A_{2223} & \sqrt{2}A_{2231} & \sqrt{2}A_{2212} \\ A_{3311} & A_{3322} & A_{3333} & \sqrt{2}A_{3323} & \sqrt{2}A_{3331} & \sqrt{2}A_{3312} \\ \sqrt{2}A_{2311} & \sqrt{2}A_{2322} & \sqrt{2}A_{2333} & 2A_{2323} & 2A_{2331} & 2A_{2312} \\ \sqrt{2}A_{3111} & \sqrt{2}A_{3122} & \sqrt{2}A_{3133} & 2A_{3123} & 2A_{3131} & 2A_{3112} \\ \sqrt{2}A_{1211} & \sqrt{2}A_{1222} & \sqrt{2}A_{1233} & 2A_{1223} & 2A_{1231} & 2A_{1212} \end{bmatrix}. \tag{A.3}$$

Writing $\boldsymbol{A}_{IJ}$ refers to the I^{th} row and J^{th} column in the modified Voigt representation.

Homogenization

For any given microstructure described by $\mathbf{C}(\mathbf{x})$, an equivalent homogeneous $\tilde{\mathbf{C}}$ tensor can be derived. With the help of a numerical scheme (FE, FFT, etc), a solution for $\boldsymbol{\sigma}(\mathbf{x}) = \mathbf{C}(\mathbf{x}) : \boldsymbol{\varepsilon}(\mathbf{x})$ can be found for any average applied strain $\bar{\varepsilon} = \langle \varepsilon(\mathbf{x}) \rangle$. By applying a pure uniaxial strain such as $\bar{\varepsilon} = [1, 0, 0, 0, 0, 0]^T$, we thus obtain the corresponding $\boldsymbol{\sigma}(\mathbf{x})$ given $\mathbf{C}(\mathbf{x})$, and the volume averaged equation $\langle \boldsymbol{\sigma}(\mathbf{x}) \rangle = \tilde{\mathbf{C}} : \langle \boldsymbol{\varepsilon}(\mathbf{x}) \rangle$ is then:

$$\begin{bmatrix} \Sigma_{11} \\ \Sigma_{22} \\ \Sigma_{33} \\ \sqrt{2}\Sigma_{23} \\ \sqrt{2}\Sigma_{13} \\ \sqrt{2}\Sigma_{12} \end{bmatrix} = \begin{bmatrix} C_{11} & \# & \# & \# & \# & \# \\ C_{21} & \# & \# & \# & \# & \# \\ C_{31} & \# & \# & \# & \# & \# \\ \sqrt{2}C_{41} & \# & \# & \# & \# & \# \\ \sqrt{2}C_{51} & \# & \# & \# & \# & \# \\ \sqrt{2}C_{61} & \# & \# & \# & \# & \# \end{bmatrix} \cdot \begin{bmatrix} 1 \\ 0 \\ 0 \\ 0 \\ 0 \\ 0 \end{bmatrix} \tag{A.4}$$

(The symbol # denotes irrelevant values). The first column in $\tilde{\mathbf{C}}$ is then inferred from the average stress $\langle \boldsymbol{\sigma}(\mathbf{x}) \rangle$ as :

$$\Big[C_{11}, C_{21}, C_{31}, C_{41}, C_{61}, C_{51} \Big]^T = \Big[\Sigma_{11}, \Sigma_{22}, \Sigma_{33}, \Sigma_{23}, \Sigma_{13}, \Sigma_{12} \Big]^T \tag{A.5}$$

Performing this procedure for the 3 uniaxial loadings and the 3 pure shear yields the entire $\tilde{\mathbf{C}}$ tensor for the microstructure at hand.

B. Moulinec's algorithm

The local deformation can be written as the sum of a constant term $\mathbf{E}$, and a fluctuating term $\boldsymbol{\varepsilon}(\mathbf{u}^*(\mathbf{x}))$, as: $\boldsymbol{\varepsilon}(\mathbf{u}(\mathbf{x})) = \boldsymbol{\varepsilon}(\mathbf{u}^*(\mathbf{x})) + \mathbf{E}$, or equivalently: $\mathbf{u}(\mathbf{x}) = \mathbf{u}^*(\mathbf{x}) + \mathbf{E} \cdot \mathbf{x}$. Here $\mathbf{u}^*$ is considered periodic, and the stress term $\boldsymbol{\sigma}$ is antiperiodic: $\boldsymbol{\sigma}(L) \cdot \mathbf{n} = -\boldsymbol{\sigma}(-L) \cdot \mathbf{n}$ so that the traction term $\boldsymbol{\sigma} \cdot \mathbf{n} = \mathbf{0}$ at the boundary (equilibrium condition). $\mathbf{n}$ is the vector normal to the boundary, and the unit cell has side of length $2L$.

The classical elasticity equation becomes:

$$\begin{cases} \boldsymbol{\sigma}(\mathbf{x}) = \mathbf{C}(\mathbf{x}) : \Big(\boldsymbol{\varepsilon}(\mathbf{u}^*(\mathbf{x})) + \mathbf{E}\Big) & \forall\, \mathbf{x} \in V \\ \nabla \cdot \boldsymbol{\sigma}(\mathbf{x}) = \mathbf{0} & \forall\, \mathbf{x} \in V \end{cases} \tag{B.1}$$

We pose a reference media with stiffness $\mathbf{C}_0$ and define $\delta_{\mathbf{C}(\mathbf{x})} = \mathbf{C}(\mathbf{x}) - \mathbf{C}_0$. Inserting $\delta_{\mathbf{C}(\mathbf{x})}$ into equation (B.1) gives:

$$\boldsymbol{\sigma}(\mathbf{x}) = (\delta_{\mathbf{C}(\mathbf{x})} + \mathbf{C}_0) : \boldsymbol{\varepsilon}(\mathbf{u}(\mathbf{x})) \tag{B.2}$$

$$= \mathbf{C}_0 : \boldsymbol{\varepsilon}(\mathbf{u}(\mathbf{x})) + \delta_{\mathbf{C}(\mathbf{x})} : \boldsymbol{\varepsilon}(\mathbf{u}(\mathbf{x})). \tag{B.3}$$

$$\text{We define: } \tau(\mathbf{x}) = \delta_{\mathbf{C}(\mathbf{x})} : \boldsymbol{\varepsilon}(\mathbf{u}(\mathbf{x})), \tag{B.4}$$

called the *polarization*, which contains the position-dependent stiffness through $\delta_{\mathbf{C}(\mathbf{x})}$, and the "random" component of deformation through $\boldsymbol{\varepsilon}(\mathbf{u}(\mathbf{x}))$. This formulation is termed the periodic Lippmann-Schwinger equation [73]. The Moulinec algorithm iteratively solves for this $\tau(\mathbf{x})$ through a fixed-point scheme.

Expessing equation (B.3) in the Fourier domain, it is possible to write the solution as:

$$\boldsymbol{\varepsilon}(\mathbf{u}^*(\mathbf{x})) = -\boldsymbol{\Gamma}^0 * \tau(\mathbf{x}) \tag{B.5}$$

where $\boldsymbol{\Gamma}^0$ is the Green operator corresponding to the reference media $\mathbf{C}_0$, and $*$ denotes a convolution product. In the Fourier domain, $\boldsymbol{\Gamma}^0$ can be derived explicitly, and takes the following form for isotropic symmetries [62, 74]:

$$\hat{\boldsymbol{\Gamma}}^0_{khij}(\boldsymbol{\xi}) = \frac{1}{4\mu_0|\boldsymbol{\xi}|^2}\Big(\delta_{ki}\xi_h\xi_j + \delta_{hi}\xi_k\xi_j + \delta_{kj}\xi_h\xi_i + \delta_{hj}\xi_k\xi_i\Big) - \frac{\lambda_0 + \mu_0}{\mu_0(\lambda_0 + 2\mu_0)}\frac{\xi_i\xi_j\xi_k\xi_h}{|\boldsymbol{\xi}|^4} \tag{B.6}$$

where δ_{ij} is the Kroeneker delta, $\boldsymbol{\xi}$ are the frequency domain variables and μ_0 and λ_0 are the Lamé coefficients of the reference material. The work of Mura [74] details the derivation of the Green operator for other material symmetries.

The principle behind the Moulinec algorithm is to use equations (B.4-B.5), respectively in the real and Fourier space, to iteratively solve equation (B.3). A constant deformation $\mathbf{E}$ is applied, and the stiffness tensors $\mathbf{C}(\mathbf{x})$ and $\mathbf{C}_0$ are known. we start by computing $\boldsymbol{\sigma}$ and $\tau(\mathbf{x})$ from $\mathbf{C}(\mathbf{x})$ and $\mathbf{E}$ (equations (B.9-B.10)). This initial $\tau(\mathbf{x})$ will not be accurate, as it only accounts for the average displacement $\mathbf{E}$. It can be used to arrive at a better estimate of $\hat{\boldsymbol{\varepsilon}}$ (equation (B.13)), which in turn yields a better estimate of $\boldsymbol{\sigma}$ (equation (B.15). The entire algorithm is repeated until the solution has converged (equation B.12), meaning the estimated error is inferior to a prescribed value. The error at iteration i is defined as:

$$e^i = \frac{\left(\left\langle |\nabla \cdot \boldsymbol{\sigma}^i|^2 \right\rangle\right)^{1/2}}{\left\langle |\boldsymbol{\sigma}^i| \right\rangle} = \frac{\left(\left\langle |\boldsymbol{\xi} \cdot \hat{\boldsymbol{\sigma}}^i|^2 \right\rangle\right)^{1/2}}{\left\langle |\hat{\boldsymbol{\sigma}}^i| \right\rangle}, \tag{B.7}$$

where $|\cdot|$ is the Euclidean norm, and $\langle\cdot\rangle$ is the spatial average. A typical value of stopping criteria is $e \leq 10^{-4}$. The main algorithm is as follows:

Initialization (step i=0)
$$\boldsymbol{\varepsilon}^0(\mathbf{x}) = E \quad \forall \mathbf{x} \in V \tag{B.8}$$
$$\boldsymbol{\sigma}^0(\mathbf{x}) = \mathbf{C}(\mathbf{x}) : \boldsymbol{\varepsilon}(\mathbf{x})^0 \quad \forall \mathbf{x} \in V \tag{B.9}$$

Iteration (step i+1)
$$a)\ \tau^i(\mathbf{x}) = \boldsymbol{\sigma}^i(\mathbf{x}) - \mathbf{C}_0 : \boldsymbol{\varepsilon}^i(\mathbf{x}) \tag{B.10}$$
$$b)\ \hat{\tau}^i(\boldsymbol{\xi}) = \mathcal{F}(\tau(\mathbf{x})^i) \tag{B.11}$$
$$c)\ \text{Convergence test} \tag{B.12}$$
$$d)\ \hat{\boldsymbol{\varepsilon}}^{i+1}(\boldsymbol{\xi}) = -\hat{\boldsymbol{\Gamma}}^0(\boldsymbol{\xi}) : \hat{\tau}(\mathbf{x})^i(\boldsymbol{\xi}) \quad \forall \boldsymbol{\xi} \neq 0, \text{ and } \hat{\boldsymbol{\varepsilon}}^{i+1}(0) = E \tag{B.13}$$
$$e)\ \boldsymbol{\xi}^{i+1} = \mathcal{F}^{-1}(\hat{\boldsymbol{\varepsilon}}^{i+1}) \tag{B.14}$$
$$f)\ \boldsymbol{\sigma}^{i+1}(\mathbf{x}) = \mathbf{C}(\mathbf{x}) : \boldsymbol{\varepsilon}^{i+1}(\mathbf{x}) \tag{B.15}$$

Once an equilibrium condition has been reached, if the applied strain $\mathbf{E}$ was chosen to be uniaxial and unitary, one column of the homogenized stiffness tensor $\tilde{\mathbf{C}}$ is obtained directly from $<\boldsymbol{\sigma}(\mathbf{x})>$ (see Appendix A).

The Moulinec basic algorithm is known to have poor convergence for the cases of high property contrasts, and in the presence of voids (infinite contrasts), as the number of iterations required is proportional to the contrast between phases [35, 75]. To deal with this problem, Eyre and Milton [75] proposed a modification to deal with the cases of high contrasts.

Multiscale Fast Fourier Transform homogenization of additively manufactured fiber reinforced composites from component-wise description of morphology[⋆]

Facundo Sosa-Rey[a,*], Clement Vella[a], Alessandra Lingua[a], Juliette Pierre[a], Nicola Piccirelli[b], Daniel Therriault[a] and Martin Lévesque[a,**]

[a] *Laboratory for Multiscale Mechanics, Polytechnique Montréal, Montreal, H3C3A7, Canada*
[b] *Safran Composites, A Technology Platform of Safran Tech, Itteville, 91760, France*

ARTICLE INFO

Keywords:
Multiscale modelling
Short-fiber composites
3-D Printing
X-ray computed tomography
Anisotropy

ABSTRACT

The process-structure-property relationship in short-fiber reinforced composites made in Fused Filament Fabrication (FFF) remains inadequately understood, much trial-and-error and extensive testing is required to use these materials for load-bearing applications. As a consequence, the largely empirical design process has hindered the adoption of this technology, notably due to the lack of reliable structural analysis capability. In order to surpass the limitations of mechanical property prediction using simplified artificial microstructures, this work demonstrates the decisive advantage of using geometries obtained directly from imaging of printed specimen instead. The analysis of μCT images is performed via a purpose-built extraction tool called OpenFiberSeg, yielding profound insight into the process-structure relation. The use of real microstructures is shown to considerably improve the mechanical behavior prediction capability via dual-scale FFT-based homogenization, bringing relative error margins below 5%, for full anisotropic description. It also becomes possible to investigate the effect of processing parameters such as nozzle diameter and printing pattern on morphological properties and on mechanical behavior, revealing the magnitude of the spatial variation of local properties. The combination of experimental and simulation enables insight that is not accessible to either alone. Original imaging data and source code are made publicly available.

---

1. Effect of processing on microstructure: radial dependence of fiber properties

The non-uniform distribution of fiber properties through an extrusion bead has been suggested by several modelling-based studies. These models predict a radial variation of fiber alignment at nozzle tip. Heller et al. [1] found it is maximized at the periphery for CF filled ABS, $v_f = 15\%$, with aspect ratio of 15, using a nozzle diameter $D = 0.35$ mm. Wang et al. [2] found that alignment is maximized at the center of the bead for a large (3 mm) nozzle used in Large Area Additive Manufacturing (LAAM), using a realistic length distribution of fibers in 13% Acrylonitrile Butadiene Styrene (ABS). Lewicki et al. [3] performed flow simulations using discretely modelled fibers and epoxy resin (a thermosetting polymer), with a $v_f = 6\%$ and aspect ratio of 50. They found that alignment is promoted during the extrusion phase, most notably close

---

[⋆] This research project is funded by the Canadian National Science and Engineering Research Council and Safran Tech.

[*] Corresponding author
[**] Principal corresponding author
`facundo.sosa-rey@polymtl.ca` (Facundo Sosa-Rey); `martin.levesque@polymtl.ca` (Martin Lévesque)
ORCID(s): 0000-0003-1140-0635 (Facundo Sosa-Rey)

to the walls. Bertevas et al. studied the impact of fiber aspect ratio and v_f on the flow-induced orientations, finding that printing beads exhibit skin-core alignment differential, also predicting higher alignment at perimeter for fiber-filled PLA [4]. They comment on the lack of rich experimental data to corroborate their findings against. Wang et al. used a fully coupled model in which the effect of fiber presence on the flow characteristic is accounted for, and compare with a weakly-couple approach, in the context of large nozzles used in LAAM [2]. They found that both models predict increased alignment at the walls, and decreased alignment at the center, but less so in the fully coupled model.

Experimental measurements of radial dependence

By knowing the position of each fiber or pore relatively to the axis of each cylindrical extrudate specimen, the radial dependence of fiber alignment, fiber length and fiber and pore densities can be computed. Those statistics are presented in Figure 1. Contrary to what was predicted in the literature [1–3], only some curves show some radial dependence, notably the higher fiber lengths at the periphery of the $D = 0.4$ mm nozzle and its more centralized porosity distribution. The porosity is higher for that nozzle as well, and is much more lateralized for both the $D = 0.25$ mm and $D = 0.8$ mm extrudates. We do not have a clear explanation for this observation at this stage, given that the input filament has evenly distributed porosity and that the extrusion speeds and temperatures used are all identical. However, the effect is seen consistently across many specimens.

2. Cumulative sum of morphological properties

Once the properties of each fiber have been extracted, the spatial variations of fiber properties can be investigated with the following method, as shown in Video 1. For the volume under consideration, the numerical value of the property of each fiber (e.g. fiber length or alignment with the x direction) is inserted at the location where that fiber is present (or NaN where matrix or porosity is present). Then, the cumulative sum of those properties all 2D slice across the volume along one of the reference directions is taken, and for each column of pixels along that direction, the sum is divided by the number of pixels containing fiber in that column of voxels. This is so that the value isn't skewed by the absence of fibers in some regions, for instance where mesoscale porosity is dominant. As a reminder, x and y are the 0° and 90° printing direction, respectively, the $x - y$ plane is the printing bed plane, and z is the vertical direction. This procedure is illustrated in Video 1

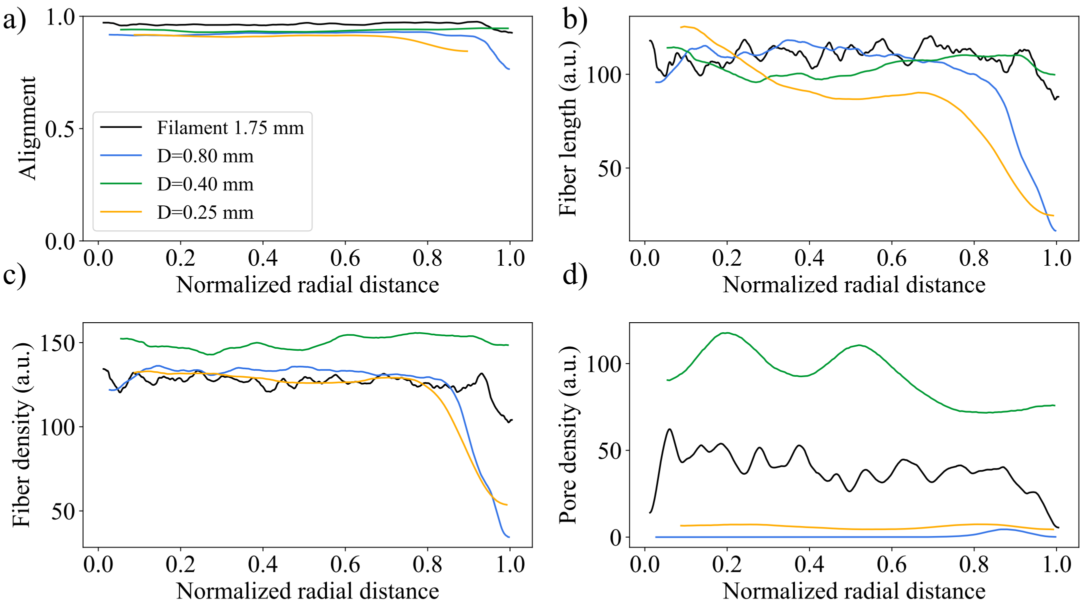

Figure 1: Variation of fiber characteristic as a function of radial position in free-space extrusion, for 3 nozzle diameters D, and the feedstock filament. a) Alignment with print direction (1.0 is perfect alignment ($\theta = 0°$), 0.0 is perpendicular ($\theta = 90°$)) is highest in the 1.75 mm filament, and has no appreciable radial dependence in any of the 4 cases. b) Fiber lengths has little radial dependence: is slightly higher at the periphery in the $D = 0.4$ mm nozzle, and slightly lower at the periphery in the $D = 0.8$ mm nozzle. c) Fiber density is evenly distributed for all nozzle diameters. d) Pore density is slightly more centralized in feedstock filament and the $D = 0.4$ mm nozzle, and much lower and more lateralized for nozzles of $D = 0.25$ mm and $D = 0.8$ mm

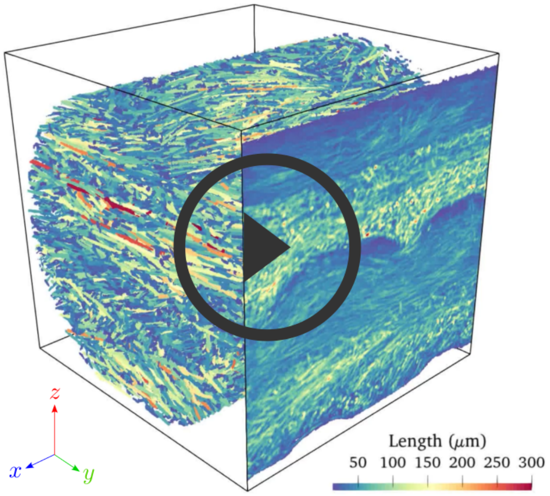

Video 1: Material property visualization by taking cumulative sum along x and y direction, for a specimen printed with the 0°-90° pattern and the $D = 0.4$ mm nozzle. Local property variability is exposed. Video available at github.com/lm2-poly/OpenFiberSeg/blob/main/MaterialProperties_cumulativeSums.mp4

References

[1] B. P. Heller, D. E. Smith, D. A. Jack, Effects of extrudate swell and nozzle geometry on fiber orientation in fused filament fabrication nozzle flow, Additive Manufacturing 12 (2016) 252–264.

[2] Z. Wang, D. E. Smith, D. A. Jack, A statistical homogenization approach for incorporating fiber aspect ratio distribution in large area polymer composite deposition additive manufacturing property predictions, Additive Manufacturing 43 (2021)

102006.

[3] J. P. Lewicki, J. N. Rodriguez, C. Zhu, M. A. Worsley, A. S. Wu, Y. Kanarska, J. D. Horn, E. B. Duoss, J. M. Ortega, W. Elmer, et al., 3d-printing of meso-structurally ordered carbon fiber/polymer composites with unprecedented orthotropic physical properties, Scientific reports 7 (2017) 1–14.

[4] E. Bertevas, J. Férec, B. C. Khoo, G. Ausias, N. Phan-Thien, Smoothed particle hydrodynamics (sph) modeling of fiber orientation in a 3d printing process, Physics of Fluids 30 (2018) 103103.